Systematic Evaluation of the Impact of Assimilating a Network of Ground-Based Remote Sensing Profilers for Forecasts of Nocturnal Convection Initiation during PECAN

SAMUEL K. DEGELIA,[a] XUGUANG WANG,[a] DAVID J. STENSRUD,[b] AND DAVID D. TURNER[c]

[a] *School of Meteorology, University of Oklahoma, Norman, Oklahoma*
[b] *Department of Meteorology and Atmospheric Science, The Pennsylvania State University, University Park, Pennsylvania*
[c] *NOAA/Earth System Research Laboratory, Boulder, Colorado*

(Manuscript received 16 April 2020, in final form 17 September 2020)

ABSTRACT: Nocturnal convection is often initiated by mechanisms that cannot be easily observed within the large gaps between rawinsondes or by conventional surface networks. To improve forecasts of such events, we evaluate the systematic impact of assimilating a collocated network of high-frequency, ground-based thermodynamic and kinematic profilers collected as part of the 2015 Plains Elevated Convection At Night (PECAN) experiment. For 13 nocturnal convection initiation (CI) events, we find small but consistent improvements when assimilating thermodynamic observations collected by Atmospheric Emitted Radiance Interferometers (AERIs). Through midlevel cooling and moistening, assimilating the AERIs increases the fractions skill score (FSS) for both nocturnal CI and precipitation forecasts. The AERIs also improve various contingency metrics for CI forecasts. Assimilating composite kinematic datasets collected by Doppler lidars and radar wind profilers (RWPs) results in slight degradations to the forecast quality, including decreases in the FSS and traditional contingency metrics. The impacts from assimilating thermodynamic and kinematic profilers often counteract each other, such that we find little impact on the detection of CI when both are assimilated. However, assimilating both datasets improves various properties of the CI events that are successfully detected (timing, distance, shape, etc.). We also find large variability in the impact of assimilating these remote sensing profilers, likely due to the number of observing sites and the strength of the synoptic forcing for each case. We hypothesize that the lack of flow-dependent methods to diagnose observation errors likely contributes to degradations in forecast skill for many cases, especially when assimilating kinematic profilers.

KEYWORDS: Deep convection; Profilers, atmospheric; Remote sensing; Forecast verification/skill; Data assimilation; Numerical weather prediction/forecasting

1. Introduction

While conventional rawinsondes provide data only a few times per day, convective-scale environments often evolve on the order of minutes to hours (Orlanski 1975). To alleviate this data gap, the meteorological community has recently pushed to expand current observing capabilities into a Nationwide Network of Networks (National Research Council 2009; Stalker et al. 2013). Part of this proposal involves the introduction of ground-based remote sensing profilers to provide high-frequency observations of the lower troposphere. Although their errors are often larger than corresponding in situ measurements, remote sensing instruments can provide thermodynamic and kinematic data multiple times per hour. Additionally, as various studies show that short-term forecasts of convection are highly sensitive to small changes in the mesoscale environment (e.g., Crook 1996; Martin and Xue 2006), assimilating such instruments can potentially have large benefits for convective-scale NWP. Recent field campaigns have employed both thermodynamic and kinematic remote sensing profilers to evaluate their potential impact for NWP systems, including the Atmospheric Emitted Radiance Interferometer (AERI; Feltz et al. 2003; Turner and Löhnert 2014), radar wind profilers (RWPs; Ecklund et al. 1988), and Doppler lidars (Menzies and Hardesty 1989).

AERIs retrieve thermodynamic profiles from observations of downwelling infrared radiance (Turner and Löhnert 2014) and have been employed to study a variety of meteorological phenomena including the African monsoon (Hansell et al. 2010), shallow convective clouds (Fast et al. 2019), atmospheric bores (Toms et al. 2017), low-frequency gravity waves (Adams-Selin and Schumacher 2019), and nocturnal convection (Geerts et al. 2017). They can capture thermodynamic data on the order of minutes, allowing for the rapid monitoring of elevated mixed layers (Feltz et al. 2003) and boundary layer stability (Blumberg et al. 2017). Recently, Turner and Blumberg (2019) introduce an optimal estimation retrieval algorithm (AERIoe) that allows for computing unique uncertainty profiles for AERI observations, improving the potential impact of assimilating this dataset by allowing for less confident retrievals, such as those in cloudy

Corresponding author: Samuel K. Degelia, sdegelia@ou.edu

DOI: 10.1175/MWR-D-20-0118.1

conditions, to be weighted less. Vertical wind profilers, including both RWPs and Doppler lidars, are also commonly used for both forecast and research applications. Similar to Doppler weather radars, RWPs actively observe horizontal winds by measuring the radio waves produced by Bragg scattering from inhomogeneities in the thermodynamic field. Doppler lidars operate similarly, measuring light waves backscattered by smaller aerosols. These kinematic profilers can be used to measure various phenomena that conventional observations typically cannot observe with high vertical or temporal resolution, including low-level jets (LLJ; Banta et al. 2002; Smith et al. 2019) or atmospheric turbulence (Smalikho et al. 2005; Calhoun et al. 2006; O'Connor et al. 2010).

Recently, the Plains Elevated Convection At Night (PECAN; Geerts et al. 2017) experiment employed AERIs and vertical wind profilers to study nocturnal convection in the Great Plains of the United States. Nocturnal thunderstorms can produce all types of severe weather hazards including severe wind, hail, and rainfall (Reif and Bluestein 2017; Weckwerth and Romatschke 2019). Nevertheless, convection-allowing NWP systems often struggle to predict such events due in part to a lack of observations that sample the mechanisms and environments responsible for nocturnal convection (e.g., Johnson and Wang 2017; Johnson et al. 2017; Keclik et al. 2017; Stelten and Gallus 2017; Peters et al. 2017; Johnson et al. 2018; Reif and Bluestein 2018). In the Great Plains, nocturnal convection initiation (CI) most commonly occurs between 0400 and 0900 UTC (Reif and Bluestein 2017), while conventional rawinsondes are typically only launched at 0000 and 1200 UTC. Moreover, most nocturnal CI events are driven by elevated ascent mechanisms such as the LLJ or undular bores (Wilson and Roberts 2006; Weckwerth et al. 2019). Such features cannot be easily observed by conventional surface data, and various studies note the necessity of lower-troposphere profiling observations to improve this data gap (e.g., Wilson and Roberts 2006; Weckwerth and Parsons 2006; Keclik et al. 2017). Given these deficiencies, recent works show that assimilating high-frequency, remote sensing datasets can be particularly useful for improving forecasts of nocturnal convection. For example, Degelia et al. (2019; henceforth referred to as D19) show that assimilating both AERIs and kinematic profilers can enhance moisture advection and support a successful CI forecast. Additionally, Chipilski et al. (2020) find that assimilating kinematic profilers improves analyses of a nocturnal LLJ and explicit forecasts of an undular bore, such that the resulting convective forecast is also improved. Additional studies assimilating AERIs and kinematic profilers include Hu et al. (2019) and Coniglio et al. (2019) who find improvements to short-term forecasts of tornadic supercells and convective evolution, respectively.

While previous works show the benefits of assimilating ground-based remote sensing datasets for single cases (e.g., Chipilski et al. 2020; D19; Hu et al. 2019) or for single platforms (e.g., Coniglio et al. 2019), many research areas remain unexplored. For example, nocturnal convection can be generated by a variety of ascent mechanisms at different scales (Reif and Bluestein 2017; Stelten and Gallus 2017; Weckwerth et al. 2019) such that the impact of assimilating these instruments is likely case- and environment-dependent. While D19 show the benefits of assimilating the data for a large-scale frontal overrunning event, it remains unclear whether the impacts will be as large for smaller-scale events such as those initiated by gravity waves or outflow boundaries. To address this question, we expand on previous studies by using carefully designed experiments to evaluate the systematic impact of assimilating a network of high-frequency (observations available every ~5–30 min) boundary layer profilers. We explore these impacts using cases observed during the PECAN field experiment, as the variety of events provides a sufficient sample of the different convective modes and mesoscale environments responsible for nocturnal CI. Furthermore, Stalker et al. (2013) propose implementing new networks alongside existing infrastructure such as the operational rawinsonde network. Thus, this study specifically evaluates the impact of assimilating collocated rawinsondes, AERIs, and kinematic profilers. We also explore whether the impact of assimilating these data primarily result from one instrument type, or if both thermodynamic and kinematic profilers are necessary to improve forecasts of nocturnal CI.

Details on the remote sensing instruments and sensitivity experiments are presented in section 2. Section 3 discusses the system configuration and verification methods we use to evaluate the impact of assimilating these data. The systematic results for assimilating the remote sensing profilers on forecasts of nocturnal CI are found in section 4. To better understand where the impacts of assimilating these data originate, we conduct a preconvective analysis in section 5 and example cases are presented in section 6. A final summary is found in section 7.

2. Observation preprocessing and sensitivity experiments

a. *Observation preprocessing*

The PECAN instruments assimilated here include rawinsondes, AERIs, Doppler lidars, and RWPs collected from both fixed and mobile sites known as PECAN integrated sounding arrays (PISA; Table 1 and Fig. 1). Most AERI observations are retrieved using AERIoe (Turner and Löhnert 2014; Turner and Blumberg 2019), which provides estimates of observation errors, with the exception of the AERI data collected from fixed PISA 1 (FP1; the AERI data from this site is described below). The Doppler lidar processing algorithm also provides error profiles using the method described in Newsom et al. (2017). For these datasets, we assimilate the observations using inflated error profiles that are tuned to produce the best forecast for the case study described in D19. Before being assimilated, each dataset is also preprocessed using the methods described at length in D19, including "superobbing" in height (Berger 2004) and various gross error checks. The few differences in observation preprocessing between this study and D19 are detailed below.

First, as the goal of this project is to evaluate the impact of assimilating a collocated network of profiling instruments, we only assimilate data from sites that include a rawinsonde and each of the remote sensing profilers. However, only two PECAN sites feature each instrument (Table 1). To increase the potential number of sites, we treat Doppler lidars

TABLE 1. List of PECAN observing sites and instruments that are assimilated for this study. We note that the FP1 site includes three wind profilers spaced by an average of 17 km. See Fig. 1 for the location of each fixed observing site.

Site name	Location	Instruments	Reference
FP1	Lamont, OK	AERI (AERIprof)	Gero et al. (2014)
		Doppler lidar	Newsom and Krishnamurthy (2014)
		915-MHz wind profiler (3)	Muradyan (2013)
		Rawinsonde	UCAR/NCAR (2015a)
FP3	Ellis, KS	AERI (AERIoe)	Turner (2016a)
		Doppler lidar	Hanesiak and Turner (2016a)
		449-MHz wind profiler	UCAR/NCAR (2017)
		Rawinsonde	Clark (2016)
FP4	Minden, NE	AERI (AERIoe)	Turner (2016b)
		915-MHz wind profiler	UCAR/NCAR (2015b)
		Rawinsonde	UCAR/NCAR (2016a)
FP5	Brewster, KS	AERI (AERIoe)	Turner (2016c)
		915-MHz wind profiler	UCAR/NCAR (2015c)
		Rawinsonde	UCAR/NCAR (2016b)
FP6	Hesston, KS	AERI	Turner (2016d)
		Doppler lidar	Hanesiak and Turner (2016b)
		Rawinsonde	Holdridge and Turner (2015)
MP1 "CLAMPS"	Mobile	AERI	Turner (2018)
		Doppler lidar	Turner (2016e)
		Rawinsonde	Klein et al. (2016)
MP3 "SPARC"	Mobile	AERI (AERIoe)	Wagner et al. (2016b)
		Doppler lidar	Wagner et al. (2016a)
		Rawinsonde	Wagner et al. (2016c)

and RWPs as a single dataset that is henceforth referred to as "composite kinematic profilers." The observations for sites that feature both wind profilers are combined using three steps. First, the high-frequency Doppler lidar profiles are temporally averaged using the same averaging window as the collocated RWP. Then, for any vertical levels where the two wind profiles overlap, we interpolate the denser profile (usually the Doppler lidar) onto the coarser observation and the two are averaged together. The observation error variances are also averaged throughout these layers to produce the error profiles for the composite dataset. Last, observations from where the two datasets do not overlap (above or below the averaging layer) are added back into the composite kinematic profile. This combination increases the number of available assimilation sites to seven (five fixed and two mobile sites; Table 1 and Fig. 1).

Additionally, we now assimilate the AERI from the Atmospheric Radiation Measurement (ARM) Southern Great Plains (SGP; Sisterson et al. 2016) station located near Lamont, Oklahoma (known as FP1 during PECAN). This instrument operated continuously throughout PECAN and provided data for nearly every case examined here. We note that the AERI observations at FP1 are retrieved using the AERIprof retrieval algorithm (Smith et al. 1999; also called AERIplus in Feltz et al. 2003) instead of AERIoe. AERIprof differs from AERIoe by using a first guess from Rapid Refresh analyses (RAP; Benjamin et al. 2016) instead of a sounding climatology, having worse performance under low- or midlevel clouds, collecting less frequent observations (15-min as opposed to 5-min retrievals), and not producing unique observation error profiles for each observing time. To assign the observation errors for AERI profiles collected from FP1, we instead use root-mean-square differences (RMSD) between the AERI and collocated soundings (given by Fig. 5 in Feltz et al. 2003). These errors are further inflated using the same method applied to the AERIoe retrievals (D19).

b. Case selection

Weckwerth et al. (2019) describe the variety of physical processes associated with nocturnal CI events in the Great Plains of the United States including frontal overrunning, events forming near a parent MCS, bores or density currents, or pristine CI events. An overview of each category is described here, and example cases simulated here are shown in Fig. 2 for each category. Frontal overrunning events occur when southerly flow advects warm, moist air above a frontal boundary, typically resulting in large-scale CI north of the boundary (Fig. 2a). Near MCS events form in proximity of an MCS but not along a radar fine line and can include "bow and arrow" (Keene and Schumacher 2013; example in Fig. 2b) and "T-initiation" (Coniglio et al. 2011) events. Bore or density current events are also associated with a parent MCS but instead develop along a radar fine line associated with an outflow boundary (Fig. 2c). Finally, pristine CI events include convective episodes not influenced by parent convective systems or obvious frontal boundaries (Fig. 2d). Weckwerth et al. (2019) provides further details and conceptual diagrams for each type of nocturnal CI.

Given this large variety of processes responsible for nocturnal CI, the skill of a convection-allowing NWP system to predict these events likely varies significantly by case. We thus

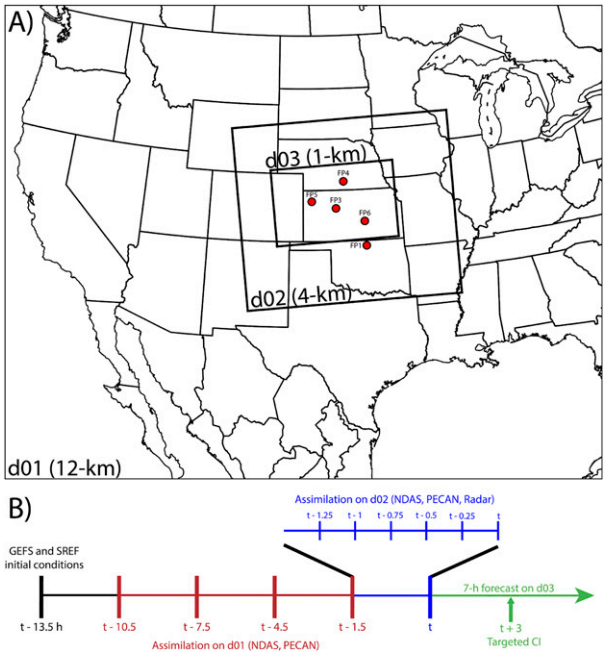

FIG. 1. Overview of experimental design including (a) domain configuration for the outer (d01, 12-km resolution) and intermediate (d02, 4-km) assimilation domains, as well as an example forecast domain (d03, 1-km) used for the 30 Jun nocturnal CI case. The forecast domain is the same size for other cases, though its exact location within d02 shifts depending on the location of the primary CI event. The location of each fixed PECAN observing site assimilated here is also overlaid. We note that two additional mobile PECAN sites are also assimilated for some cases, though their location varied by event. (b) Flowchart for the cycled assimilation, including the four 3-h assimilation cycles on d01, the six 15-min assimilation cycles on d02, and the 7-h forecast period. The primary CI event for each case (Table 2) occurs 3 h after the forecast initialization period.

explore the impact of assimilating the thermodynamic and kinematic profilers through systematic experiments that include many nocturnal CI events observed during PECAN. From the list of nocturnal CI events observed during PECAN and compiled by Weckwerth et al. (2019), we select a case for evaluation if it features 1) at least two observing sites with a rawinsonde launched between 2330 and 0030 UTC, and 2) at least one observing site that is no more than 300 km away from the center of the nocturnal CI event. These conditions ensure that we can evaluate the impact of assimilating a collocated network of remote sensing profilers alongside a representation of the current operational rawinsonde network and that the observations are close enough to impact the primary CI event. We note that while the cases are selected based on the presence of this primary CI event, we verify all observed CI events that occur within the forecast domain. After applying these conditions, we select 13 nocturnal CI cases for evaluation (Table 2). On average, the geographic center of the observing sites is located 221 km (σ = 124.1 km) away from primary nocturnal CI event. While this distance is larger than other studies that assimilate field campaign data (e.g., Chipilski et al. 2020), the cycled data assimilation allows for observation impacts to propagate far from the observing site, thus justifying the verification of all CI events within the forecast domain.

c. Experimental design

To determine the systematic impact of assimilating this collocated network of thermodynamic and kinematic profilers, we carefully design a set of data addition experiments (Table 3) based around a baseline experiment, SONDE that only features the assimilation of conventional observations and PECAN rawinsondes. We then separately assimilate collocated AERIs and composite kinematic profilers in the SONDE_TQPROF and SONDE_UVPROF experiments, respectively, by also assimilating the remote sensing data in addition to the baseline observations. To ensure that these data addition experiments demonstrate the impact of assimilating the remote sensing instruments alongside a representation of the conventional rawinsonde network, we only assimilate PECAN rawinsondes closest to 0000 UTC in all experiments. If no rawinsondes are launched from a site between 2330 and 0030 UTC, then all data from that site are excluded for that case. Finally, we assimilate all sets of collocated observations together in SONDE_ALLPROF.

3. System configuration and verification techniques

a. Model and DA system configuration

To simulate the 13 nocturnal CI events, we apply a multiscale model and DA system adapted from Degelia et al. (2018, 2019). We first generate initial and lateral boundary conditions for 40 ensemble members by downscaling forecasts from the first 20 members of both the GEFS (Wei et al. 2008) and Short-Range Ensemble Forecast (SREF; Du et al. 2014). Version 3.7.1 of WRF-ARW (Skamarock et al. 2008; parameterization schemes shown in Table 4) then integrates this information forward for use in cycled DA. The cycled DA is performed using a GSI-based ensemble Kalman filter (EnKF; Wang et al. 2013; Johnson et al. 2015; Wang and Wang 2017). Because the EnKF samples cross-variable error covariances from the background ensemble, it allows for thermodynamic observations to update the kinematic state and vice versa. Covariance localization and background error inflation methods are also utilized within the GSI-based EnKF system and are detailed in Table 4.

Although data gaps prevent the same quantity of data from being assimilated for each nocturnal CI case, we ensure that each site is at least assimilated for the same duration by always beginning DA 16.5 h prior to the primary, observed CI event (Fig. 1b; 13.5 h of DA and 3 h of forecast spinup). Four assimilation cycles are first performed every 3 h on an outer, CONUS domain (Δx = 12 km; d01 in Fig. 1) using conventional data, PECAN rawinsondes, and the PECAN remote sensing profilers to improve the analysis of synoptic and mesoscale features. The conventional data consist of operational surface, rawinsondes, aircraft, ship, and buoy observations obtained from the North American Mesoscale Data Assimilation System

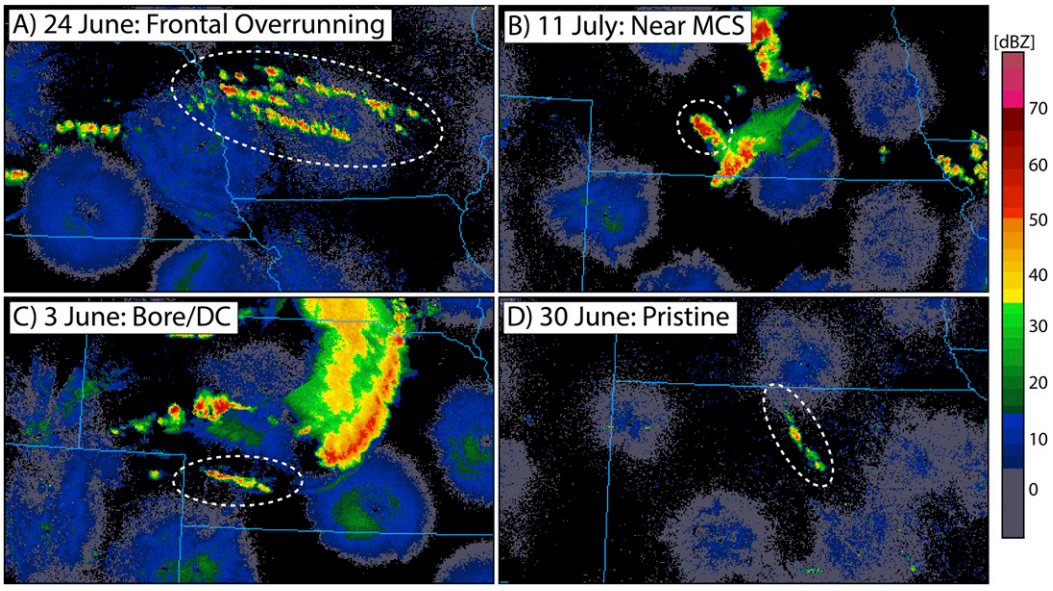

FIG. 2. Composite reflectivity (dBZ) for example nocturnal CI events from each category including (a) frontal overrunning, (b) near MCS (bow and arrow event shown), (c) bore or density current, and (d) pristine. The dashed white oval regions indicate the primary nocturnal CI events that are likely initiated by the indicated ascent mechanisms. These images are courtesy of the image archive (available online at https://www2.mmm.ucar.edu/imagearchive/) maintained by the Mesoscale and Microscale Meteorology Division (MMM) of NCAR.

(NDAS; Rogers et al. 2009). Afterward, we downscale the outer domain to an intermediate, convection-allowing grid where radar observations are also assimilated for six, 15-min cycles to improve analyses of storm-scale features (Δx = 4 km; d02 in Fig. 1). The radar observations include reflectivity and radial velocity data that have been preprocessed using WDSS-II (Lakshmanan et al. 2007). Previous studies (e.g., Johnson and Wang 2019) indicate that at least 1-km grid spacing is necessary to capture small-scale convective events such as those initiating along an undular bore. Thus, after DA is complete, we initialize 7-h forecasts from the final EnKF analysis on a 1-km forecast domain (d03 in Fig. 1). Following Johnson et al. (2020), we only use the first 10 ensemble members for the forecast period to represent current convection-allowing ensemble systems.

b. *Object-based identification of CI*

Given that CI is a locally rare and rapidly occurring process (Burlingame et al. 2017), applying traditional verification methods can be difficult (e.g., Kain et al. 2013). Recently, Burghardt et al. (2014) developed an object-based technique

TABLE 2. List of simulated nocturnal CI events and their most likely ascent mechanisms from Weckwerth et al. (2019). The strength of the large-scale ascent for each case is also denoted. CI events that develop near a 500- or 700-hPa upstream trough are classified as strongly forced, while other events are classified as weakly forced. The PECAN observing sites assimilated and their average geographic distance from the nocturnal CI event (km) are also listed for each case. Note that while these mechanisms correspond to the primary CI event used to select the cases, all CI objects occurring within the forecast period and domain are verified.

Time and date of CI	Primary CI mechanism	Strength of large-scale ascent	Sites assimilated	$\bar{d}$ (km)
0700 UTC 3 Jun	Bore or density current	Weak	5 (FP1, FP3, FP4, MP1, MP3)	389
0430 UTC 6 Jun	Near MCS	Weak	3 (FP1, FP3, FP4)	201
0600 UTC 24 Jun	Frontal overrunning	Strong	5 (FP1, FP3, FP4, FP5, MP3)	513
0300 UTC 26 Jun	Frontal overrunning	Strong	3 (FP1, FP3, FP5)	229
0900 UTC 30 Jun	Pristine	Weak	2 (FP1, FP3)	155
0430 UTC 5 Jul	Pristine	Weak	4 (FP1, FP3, FP4, MP1)	143
0630 UTC 6 Jul	Bore or density current	Strong	3 (FP1, FP4, MP1)	47
0700 UTC 9 Jul	Near MCS	Strong	2 (FP4, FP5)	358
0400 UTC 10 Jul	Near MCS	Weak	4 (FP1, FP3, FP5, MP1)	124
0530 UTC 11 Jul	Near MCS	Strong	5 (FP1, FP3, FP4, FP5, FP6)	225
0600 UTC 14 Jul	Bore or density current	Weak	5 (FP1, FP3, FP4, FP5, FP6)	223
0830 UTC 15 Jul	Near MCS	Weak	6 (FP1, FP3, FP4, FP5, FP6, MP3)	157
0430 UTC 16 Jul	Bore or density current	Strong	5 (FP1, FP3, FP4, FP5, FP6)	106

TABLE 3. List of experiments.

Experiment	Datasets assimilated
SONDE	PECAN rawinsondes launched between 2330 and 0030 UTC
SONDE_TQPROF	All observations from SONDE plus collocated thermodynamic profilers
SONDE_UVPROF	All observations from SONDE plus collocated kinematic profilers
SONDE_ALLPROF	All observations from SONDE_TQPROF and SONDE_UVPROF

that allows for detecting and matching between specific observed and forecast CI objects. We apply this method, also utilized by Burlingame et al. (2017) and Keclik et al. (2017), to identify each CI event occurring during the 7-h forecast period (example shown in Fig. 3). The same technique is simultaneously applied to both the forecasts and MRMS radar observations (Smith et al. 2016) using the following steps. First, we apply bilinear interpolation to regrid the observed MRMS reflectivity data onto the model grid for each case. We then identify convectively active regions in the forecast and observations by selecting areas of reflectivity greater than 35 dbZ at the −10°C level. Searching at the −10°C isotherm avoids potential brightbanding effects that could cause spurious CI events to be detected in stratiform precipitation regions (Gremillion and Orville 1999). For the forecast data, we calculate reflectivity at −10°C by searching downward from the model top to find the first model level where the ambient temperature is greater than −10°C. The forecast reflectivity data are then interpolated onto that height. The MRMS reflectivity at −10°C is calculated using the same method, except that RAP analyses are used for determining the height of the −10°C isotherm (NOAA 2015). We note that the height fields derived from the forecast data and RAP analyses are generally within 100 m of each other and have little impact on the derived reflectivity product.

Once convectively active regions have been identified, we detect individual convective objects by segregating the reflectivity data with a watershed transform algorithm that requires at least four contiguous grid points of reflectivity > 35 dbZ (Lakshmanan et al. 2009). These convectively active objects are then tracked backward in time so that their starting time and location (CI) can be determined. The object tracking works by searching a 15-km search radius, which we subjectively find to work well for the cases simulated here, around each object at the previous output time (15 min). This step effectively tracks objects across time by merging any pairs with a translation speed less than 60 km h^{-1}. We note that only ~2% of objects move faster than this speed, indicating that the threshold likely has little impact on the results presented herein. After tracking, we remove any objects that are not maintained for a minimum of 1 h, such that we only account for mature, deep convection (Burlingame et al. 2017). We then define the CI objects by the starting time and centroid location of these convectively active objects (red and yellow dots in Fig. 3).

c. *Object-based verification of CI*

To quantify the capability of each forecast experiment to predict CI, we apply both probabilistic and deterministic verification methods based on the CI objects detected using the previous method. The forecast probabilities are created using individual binary masks for each ensemble member. Given that CI often occurs at only a few grid points, we determine ensemble probabilities using unsmoothed neighborhood maximum ensemble probabilities (NMEP) that Schwartz and Sobash (2017) recommend for locally rare events such as updraft helicity tracks. NMEP measures the percentage of ensemble members that produce CI within a selected neighborhood. Once NMEP has been calculated for each case, we then verify the probabilistic forecast fields using fractions skill score (FSS; Roberts and Lean 2008), which measures how well each experiment predicts general regions of nocturnal CI.

TABLE 4. List of WRF-ARW and EnKF settings used for all simulations. We note that a different microphysical parameterization scheme is used for the DA and forecast periods and that no cumulus parameterization is utilized on the 4-km assimilation domain (d02 in Fig. 1). The two values shown for the localization radii represent the parameters used for the outer (12-km, d01) and intermediate (4-km, d02) assimilation domains, respectively.

Parameterization or DA setting	Scheme name or value
Microphysical parameterization (DA)	WSM6 (Hong and Lim 2006)
Microphysical parameterization (forecast)	Lin et al. (1983)
PBL parameterization	MYNN (Nakanishi and Niino 2006)
Longwave radiation parameterization	RRTMG (Iacono et al. 2008)
Shortwave radiation parameterization	Goddard (Tao et al. 2003)
LSM	Noah (Ek et al. 2003)
Cumulus parameterization	Grell and Freitas (2013)
Localization radii (conventional observations, PECAN rawinsondes, AERIs)	Horizontal (km): 700, 200 Vertical [$\ln(P/P_{ref})$]: 1.1, 0.55
Localization radii (Doppler lidars, radar wind profilers)	Horizontal (km): 700, 200 Vertical [$\ln(P/P_{ref})$]: 0.20, 0.20
Localization radii (radar observations)	Horizontal (km): N/A, 20 Vertical [$\ln(P/P_{ref})$]: N/A, 0.55
Inflation factor (prior)	1.15, decreasing to 1.03 at model top
Inflation factor (posterior)	0.95 of prior spread

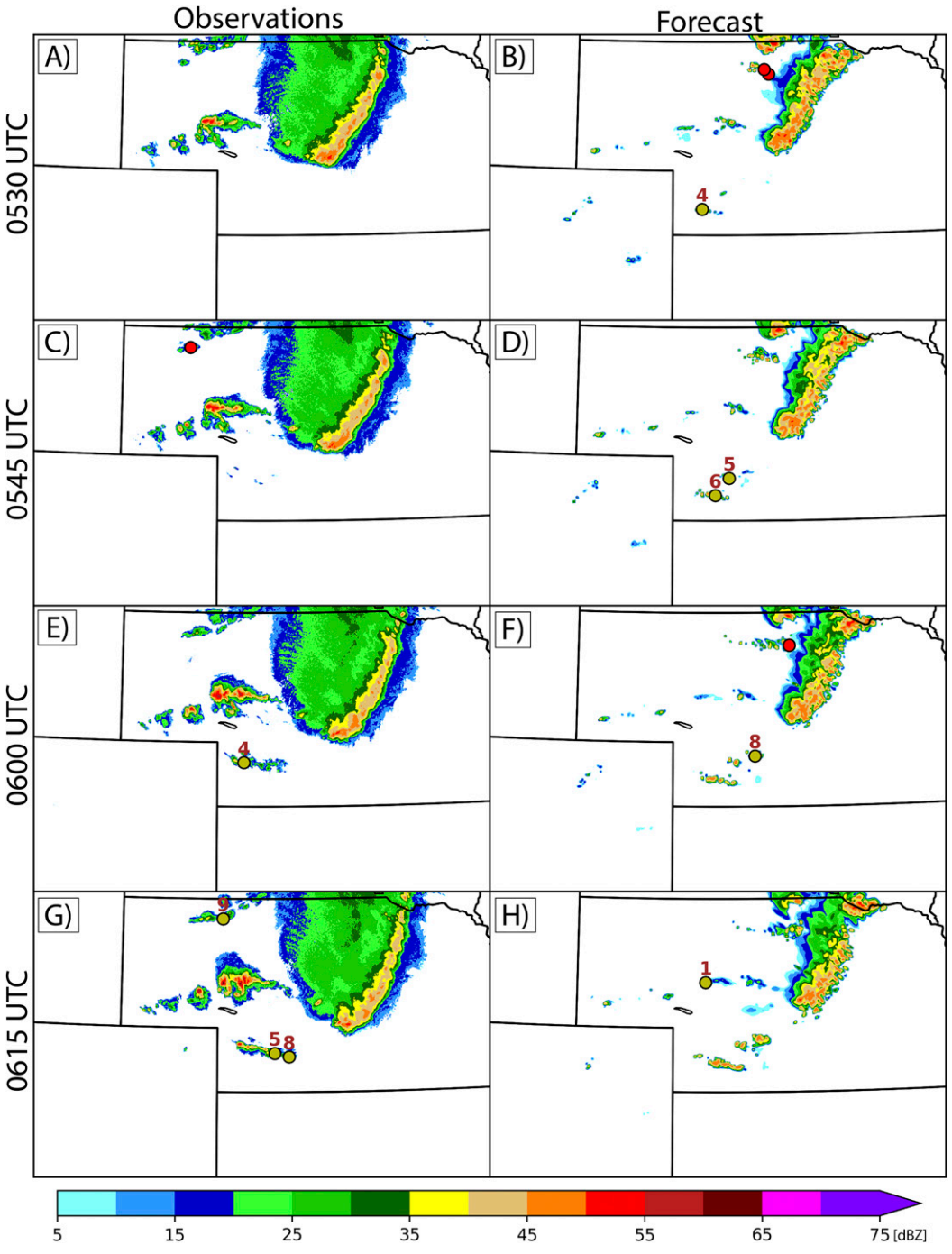

FIG. 3. Example of the object-based CI detection algorithm applied throughout this study for forecast member 1 of SONDE_ALLPROF on 3 Jun. The background shading represents the (a),(c),(e),(g) observed and (b),(d),(f),(h) forecast reflectivity at −10°C (dBZ). The unmatched CI objects, indicated at the time and centroid location of CI, are represented by red dots. If a CI object is matched between the forecast and observed objects, it is instead represented by a yellow dot and the pair ID is annotated above the object.

The deterministic verification technique (Fig. 3) matches between forecast and observed objects based on subjectively chosen spatiotemporal thresholds (Burghardt et al. 2014). We match between forecast and observed objects if 1) the centroid distance between the pair is less than 150 km, and 2) if the absolute difference in their initiation times is less than 2 h. We also perform various sensitivity tests that change these spatiotemporal thresholds and find little to no impact on the

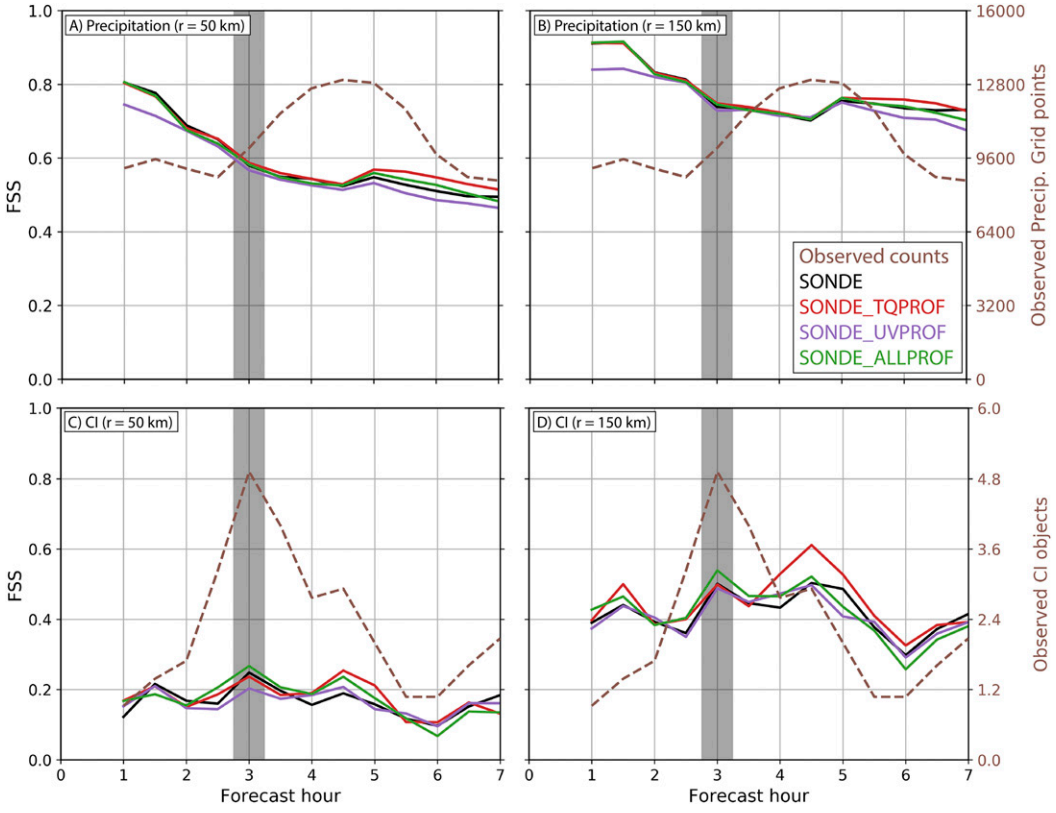

FIG. 4. Time series of fractions skill score (FSS) for varying neighborhoods. The time series is created by averaging the time series of FSS for the 13 individual CI cases. The statistics are calculated for (a),(b) hourly precipitation exceeding 6.35 mm (0.25 in.) and (c),(d) CI objects detected over the previous hour. Also shown are (a),(b) the average number of grid points where observed hourly precipitation exceeds 6.35 mm, and (c),(d) the average number of observed CI objects. While each CI event during the 7-h forecast is verified here, the timing of the primary CI event used to select the 13 cases is indicated by the gray shading.

relative performance between the assimilation experiments. If we find multiple potential matches between object pairs, then we match the pair with the lowest composite error (E; Burghardt et al. 2014), defined as

$$E = [E_d^2 + (V_c E_t)^2]^{1/2}, \quad (1)$$

where E_d is the centroid distance error, E_t is the absolute timing error, and V_c is a representative storm motion calculated by averaging the simulated wind speed between 450 and 850 hPa at the location of the observed CI object (Burlingame et al. 2017).

After matching between the forecast and observed objects (yellow dots in Fig. 3), we organize results into a 2×2 contingency table and calculate the standard verification metrics (Wilks 2011) of probability of detection (POD), false alarm ratio (FAR), bias, and critical success index (CSI). Recent studies (e.g., Skinner et al. 2016; Schwartz et al. 2017) explore various ways to compute similar object-based verification metrics across an ensemble. Here, we compute these contingency metrics by combining hits, misses, and false alarms from each forecast member into a single contingency table such that one value of each metric is computed for the ensemble per case. Consequently, the limited number of cases ($n = 13$) prevents the estimation of statistical significance. In addition to the contingency metrics, we also calculate timing, distance, speed, direction, aspect ratio, and axis angle errors of the matched object pairs following the definitions in Davis et al. (2006). We calculate the latter four attributes 1 h after CI such that the convection has had some time to evolve from its original cellular shape.

4. Systematic impact of assimilating remote sensing profiles for forecasts of nocturnal CI

We first assess the general impacts of assimilating the PECAN profilers by verifying NMEP forecasts of both hourly precipitation exceeding 6.35 mm (0.25 in.) and CI (Figs. 4, 5). In general, each experiment performs similarly for precipitation with only slight changes to the FSS when assimilating remote sensing data. Compared to SONDE, assimilating the thermodynamic profilers in SONDE_TQPROF slightly improves the mean precipitation skill at most forecast hours and for both neighborhood sizes (Figs. 4a,b). Most of the impact to the mean FSS skill in SONDE_TQPROF is a result of three cases (i.e., outliers in Figs. 5a,b). Conversely, assimilating the kinematic profilers leads to a consistent negative impact for

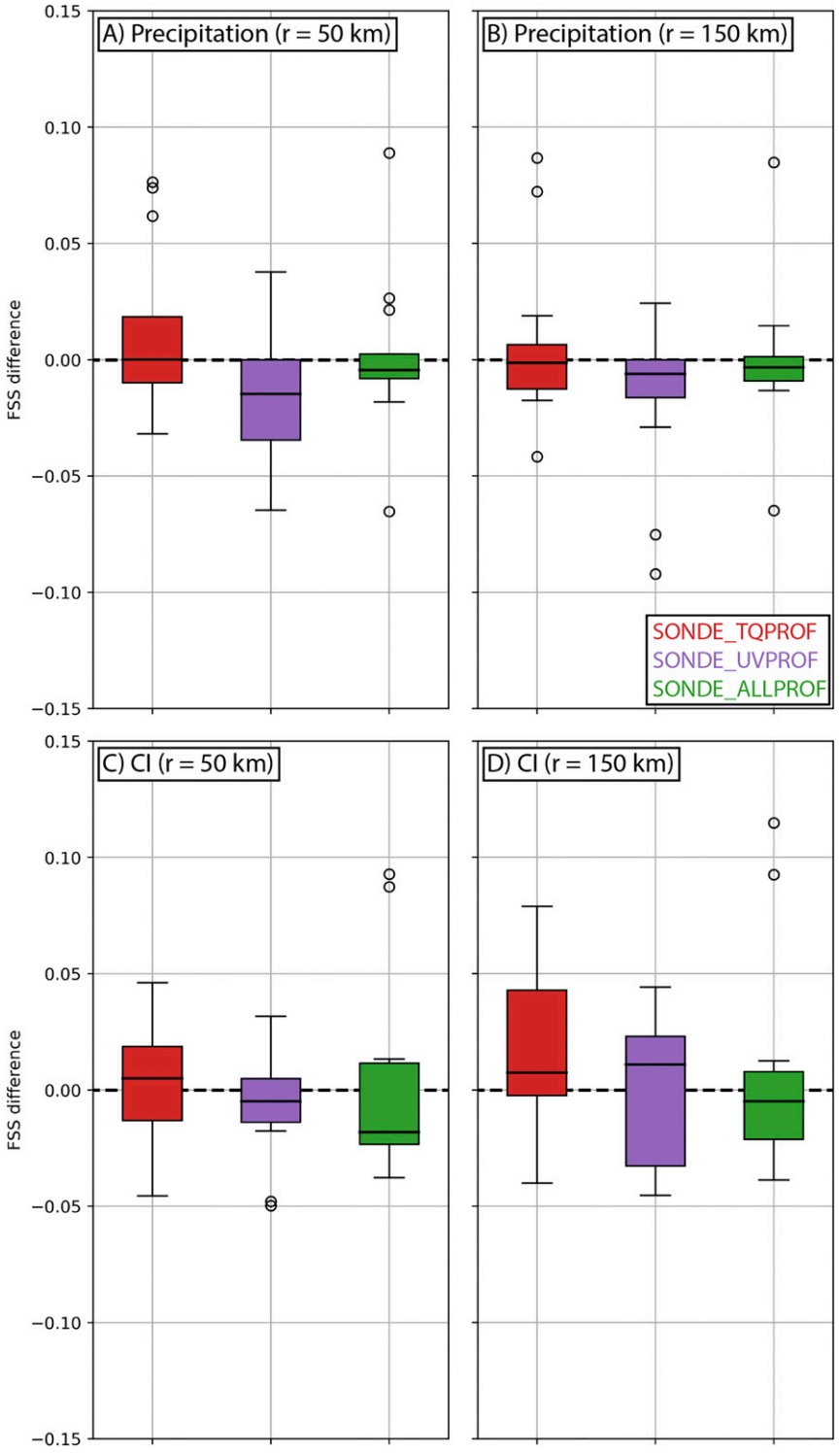

FIG. 5. Box-and-whisker plots for FSS differences between the indicated experiment and SONDE ($FSS_{EXPERIMENT} - FSS_{SONDE}$) using varying neighborhoods. The statistics are calculated for (a),(b) hourly precipitation exceeding 6.35 mm (0.25 in.) and (c),(d) CI objects detected over the previous hour. The line through the middle of the box represents the median of the data. The bottom of the box represents the lower quartile and the top of the box represents the upper quartile. The whiskers extend to the 1.5 times the interquartile range (IQR). Any outliers above or below 1.5 × IQR are plotted as circles.

TABLE 5. Mean contingency statistics for each experiment including the number of observed and forecast CI objects per case, probability of detection (POD), false alarm ratio (FAR), bias, and critical success index (CSI). The number of forecast objects is also averaged across the 10 ensemble members. POD, FAR, bias, and CSI are calculated over every nocturnal CI event within the forecast domain, while POD-primary is calculated over only the nocturnal CI events corresponding to the primary ascent mechanisms listed in Table 2.

Statistic	SONDE	SONDE_TQPROF	SONDE_UVPROF	SONDE_ALLPROF
No. of observed CI objects	15.5	15.5	15.5	15.5
No. of forecast CI objects	15.4	15.3	14.2	15.3
POD	0.53	0.54	0.50	0.52
FAR	0.48	0.48	0.47	0.50
Bias	1.13	1.09	1.04	1.14
CSI	0.34	0.35	0.33	0.33
POD-primary	0.66	0.70	0.64	0.68

precipitation. SONDE_UVPROF produces lower skill compared to SONDE, especially during the early and later forecast hours (Figs. 4a,b), leading to median FSS impacts of −0.02 to −0.01 depending on the exact neighborhood size (Figs. 5a,b). When assimilating both sets of profilers together in SONDE_ALLPROF, we find little impact to the FSS such that the negative impacts of assimilating the composite kinematic profilers likely counteract the positive impacts of assimilating the thermodynamic profilers. Additionally, though the forecasts are more skillful when verifying over a larger neighborhood, the impacts remain generally the same magnitude at both $r = 50$ and 150 km.

Similar to results found by Keclik et al. (2017), all experiments produce much lower skill for CI forecasts compared to precipitation (Figs. 4, 5). Though not necessarily surprising, this suggests that convection-allowing NWP systems can predict general regions where precipitation is likely to occur, but struggle to predict the precise timing and location of initiation within those regions. We also find that assimilating the PECAN profilers has a larger overall impact for CI compared to precipitation (Figs. 4c,d, 5c,d). Using a 50-km verification neighborhood, we find that SONDE_TQPROF produces increased skill compared to SONDE at ~4.5 h (Fig. 4c), and between 3.5 and 6.5 h when using a 150-km neighborhood (Fig. 4d). Conversely, SONDE_UVPROF often produces similar or lower skill compared to SONDE, most notably at ~3 h using a 50-km neighborhood (Fig. 4c) and at ~5 h when using a 150-km neighborhood (Fig. 4d). Again, these impacts likely cancel each other out when both datasets are assimilated, such that SONDE_ALLPROF produces similar skill to SONDE

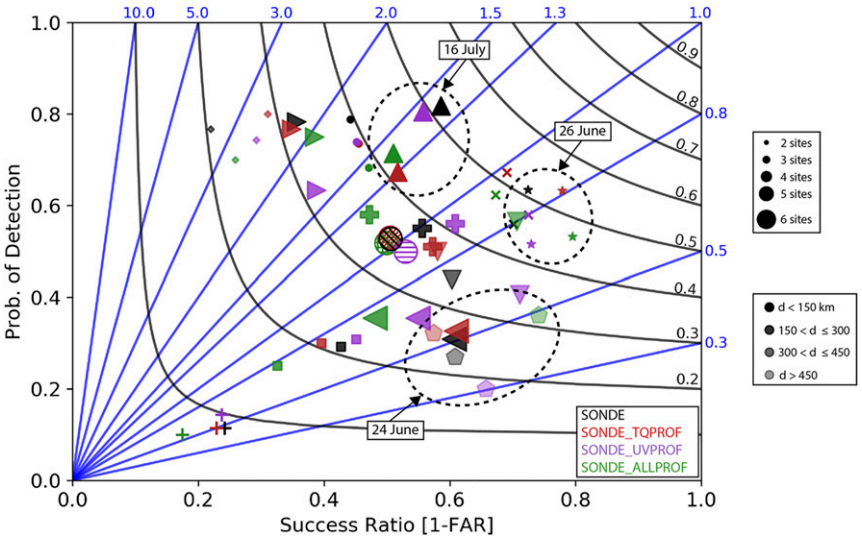

FIG. 6. Performance diagrams for each nocturnal CI case. The x axis is the success ratio (1 − false alarm ratio) and the y axis is the probability of detection. The critical success index is represented by the curved black lines and the bias is represented by the straight blue lines. The different marker styles indicate a different nocturnal CI event, while the marker size indicates the number of sites assimilated and the transparency of the maker indicates the average distance between the geographic center of the observing sites and the primary CI event of interest (Table 2). Additionally, the hatched, circular markers near the center of the plot represent the mean across all 13 nocturnal CI cases.

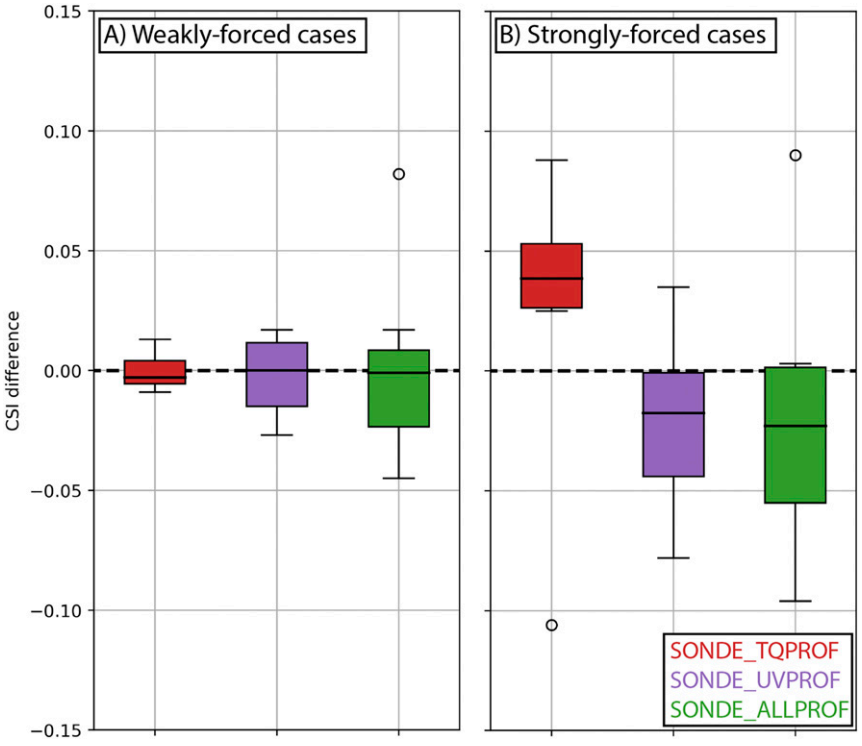

FIG. 7. As in Fig. 5, but for CSI differences between the indicated experiment and SONDE ($CSI_{EXPERIMENT} - CSI_{SONDE}$) for (a) weakly forced and (b) strongly forced cases.

(Figs. 4c,d, 5c,d). We discuss hypotheses for why assimilating kinematic data sometimes degrades the nocturnal convective forecasts in later sections. Additionally, the FSS for CI shows stronger case-to-case variability (as indicated by the taller boxes in Figs. 5c,d) and more hourly variability than the FSS for precipitation (Figs. 4c,d). The latter result is likely related to the large variability in the number of observed CI objects, as Figs. 4c and 4d shows local minimums in skill when the observed object counts decrease at forecast hour 6. These increased impacts for CI compared to precipitation suggests that nocturnal CI forecasts are more sensitive to the boundary layer modifications generated by assimilating the remote sensing data. While small changes to the low-level preconvective environment might slightly shift the location or magnitude of large-scale precipitation regions, similar changes can also cause CI forecasts to entirely fail or new CI events to occur (e.g., Martin and Xue 2006).

While the FSS metric quantifies how well each experiment predicts general regions of CI, we also perform a deterministic verification technique that matches between specific observed and forecast CI events (Table 5). This method allows us to not only compute the percentage of CI events that are successfully predicted, but also measure the number of false alarms and estimate various errors of the successful matches. We note that the "POD-primary" in Table 5 evaluates only over objects associated with the primary CI events used to select the 13 CI cases (Table 2), while the other detection statistics verify over every CI object within the model domain.

Similar to the probabilistic verification results, we find that each experiment produces similar contingency metrics with mean PODs and FARs of ~0.50, biases of ~1.10,[1] and CSIs of ~0.33 (Table 5). While the assimilation impacts to these contingency metrics are small, we find measurable impacts that agree with the findings presented for the probabilistic verification methods. First, assimilating the thermodynamic retrievals in SONDE_TQPROF produces the best results for many contingency metrics. Compared to SONDE, SONDE_TQPROF leads to small increases in POD (+0.01), POD-primary (+0.04), and CSI (+0.01), and a small decrease in the bias (−0.04). Conversely, assimilating the kinematic profilers produces the worst overall metrics for POD, CSI, and POD-primary. SONDE_ALLPROF performs similarly to SONDE, indicating that positive and negative impacts of assimilating the two datasets again counteract each other. We note the average POD is slightly higher when verifying over objects associated with the primary CI events targeted by the data assimilation (~0.64). In addition to being located closer to the mobile observations, these events are often the largest within the domain and are likely easier to capture. However, the impact on the rest

[1] The mean bias for each experiment is greater than 1.0 despite a lower average number of forecast objects compared to observed objects. This is due to most cases featuring a bias less than 1.0, but three cases producing many forecast objects where the individual bias for that case is greater than 1.6.

TABLE 6. Mean attribute errors for the successful matches (hits) of each nocturnal CI event. All errors are calculated as (forecast attribute − observed attribute) and all errors except for distance can be either positive or negative. The timing and distance errors are calculated at the valid time for CI, while the speed, direction, aspect ratio, and axis angle errors are calculated 1 h after CI such that the convection has had some time to develop from its original cellular shape.

Mean error	SONDE	SONDE_TQPROF	SONDE_UVPROF	SONDE_ALLPROF
Timing (min)	2.5	3.5	−1.1	0.2
Distance (km)	70.4	68.9	69.2	65.5
Speed (m s^{-1})	−0.2	−0.2	−0.4	−0.1
Direction (°)	13.4	12.4	14.3	12.4
Aspect ratio	0.04	0.04	0.02	0.07
Axis angle (°)	−9.6	−9.0	−8.3	−2.6

of contingency statistics generally do not change when limited to the primary CI events (not shown).

We also present performance diagrams (Roebber 2009) for each individual CI case in Fig. 6. In general, we find strong case-to-case variability in both the baseline performance and for the impact of assimilating the remote sensing profilers. For example, SONDE_ALLPROF shows a large increase in CSI compared to SONDE for the 24 June frontal overrunning case (pentagons in Fig. 6). However, assimilating both datasets together has the opposite impact for the 26 June frontal overrunning case (stars in Fig. 6). Likewise, we also find a few cases where assimilating the thermodynamic data degrades the forecast skill (e.g., 16 July given by triangles in Fig. 6) despite the mean contingency impacts being positive. Romine et al. (2016) find similar results when assimilating dropsonde data, noting that the cases with the most positive impacts feature

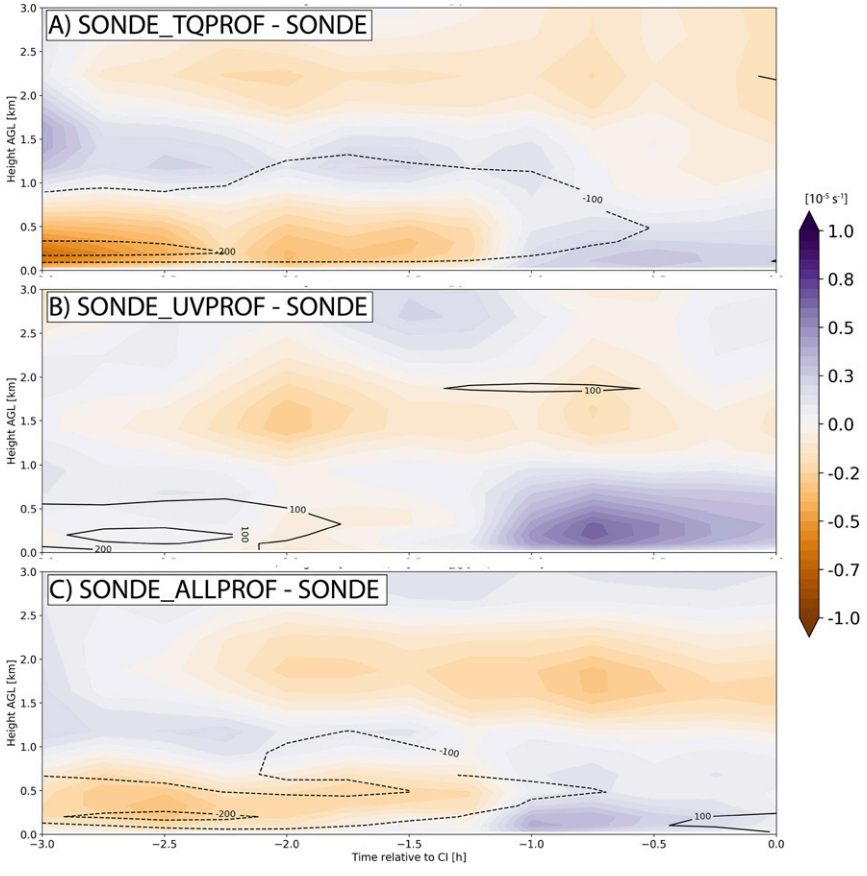

FIG. 8. Composite, or mean, time–height cross sections for differences in divergence ($10^{-5}\,s^{-1}$; shading) and Δz_{LFC} (m; contours) between SONDE and other experiments. The cross sections are averaged over a 75-km radius around the observed CI event. The cross sections are also plotted relative to the observed timing of CI such that the final point on the x axis indicates CI.

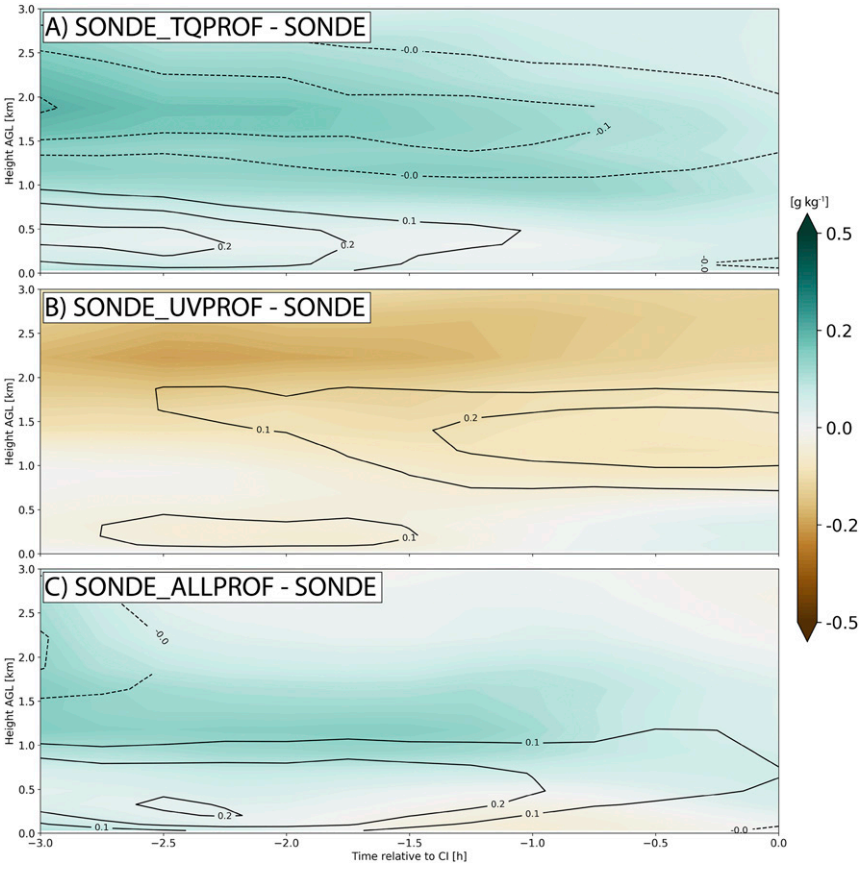

FIG. 9. As in Fig. 8, but for differences in water vapor mixing ratio (g kg^{-1}; shading) and temperature (°C; contours).

observations that sample broad regions around the event of interest. Thus, the case-to-case variability shown here is likely sensitive to both the number of observing sites assimilated and their location relative to the CI event (see marker size and transparency in Fig. 6). We also compare the impact of assimilating the remote sensing data to the strength of synoptic-scale ascent (Fig. 7). Cases that feature an upstream trough at either 500 or 700 hPa are classified as strongly forced (6 out of 13 cases), while other events are classified as weakly forced (7 out of 13 cases). This subjective analysis reveals that most of the impact to the mean CSI in SONDE_TQPROF results from assimilating the AERI data for strongly forced cases (Fig. 7b). Instead, assimilating the AERI observations for weakly forced cases produces little-to-no impact, suggesting that much of the case-to-case variability could also be related to the synoptic regime that the nocturnal CI events develop within.

Finally, we also calculate mean attribute errors for the successful matched pairs (Table 6). We note that the timing and distance errors shown are likely biased, as an event would only be included in this calculation if it passed certain thresholds of these errors to be considered a match. Overall, each experiment produces near zero mean timing errors. Although this result agrees with previous evaluations of CI forecasts (Johnson et al. 2017; Kain et al. 2013), we note that the mean absolute timing error for each experiment is ~45 min (not shown), indicating that NWP forecasts still struggle to predict the precise timing of CI. Each experiment also produces a distance error of ~70 km, which is slightly larger than previous studies (e.g., ~50 km in Keclik et al. 2017), though these exact values are likely sensitive to the specific ascent mechanism for each CI event. When assimilating the thermodynamic profilers, the experiments show small improvements to the distance, direction, and axis angle errors. Assimilating the composite kinematic profilers also slightly improves the timing, distance, aspect ratio, and axis angle errors. When both datasets are assimilated in SONDE_ALLPROF, the forecasts produce the lowest errors in timing, distance, direction, and axis angle. Thus, while we find that the impacts of assimilating the two profiler networks counteract each other for detection of CI, we instead find improvements to the attributes of the CI event when assimilating both thermodynamic and kinematic data together.

5. Preconvective analysis of observation impacts

To better understand why assimilating the thermodynamic profilers results in better forecasts of nocturnal CI

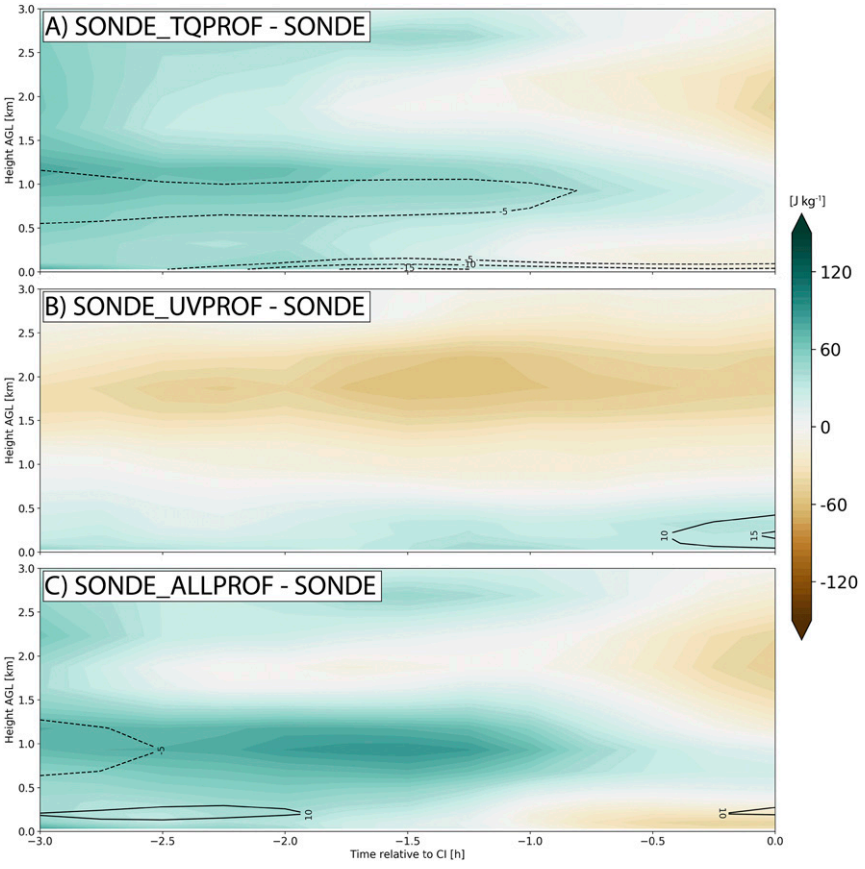

FIG. 10. As in Fig. 8, but for differences in CAPE (J kg^{-1}; shading) and CIN (J kg^{-1}; contours). Negative values of CIN represent a decrease in inhibition for that experiment compared to SONDE.

and precipitation, and why assimilating the kinematic datasets often degrades these forecasts, we create composite time–height cross sections leading up to the CI event. The cross sections are formed by averaging each case and ensemble member over a 75-km radius centered on the primary observed CI event to capture the average distance error between forecast and observed objects (Table 5). We then plot differences in the convective ingredients (Johns and Doswell 1992) between SONDE and other experiments in Figs. 8–10.

In general, separately assimilating the collocated profilers has similar impacts on the midlevel divergence (Figs. 8a,b). Both the thermodynamic and kinematic profilers enhance the midlevel ascent during the 2 h period prior to CI (i.e., reduced divergence in Figs. 8a,b), though SONDE_TQPROF enhances the ascent in a slightly higher layer (1.5–3 km AGL) compared SONDE_UVPROF (1–2 km AGL). We note that the increased low-level divergence in all figures ~1 h prior to CI is likely a result of stronger cold pools and their associated downdrafts compared to SONDE. As Wilson and Roberts (2006) show that most nocturnal convective events develop in environments featuring midlevel convergence, the impacts shown here indicate that assimilating both sets of profilers generally yields a preconvective environment that is more supportive of nocturnal CI. When both sets of profilers are assimilated together, SONDE_ALLPROF (Fig. 8c) shows an elevated divergence field similar to the individual experiments. Therefore, both datasets likely improve similar deficiencies in the ascent forecast by SONDE such that there is no significant change when assimilating the profilers together.

While the remote sensing profilers make similar modifications to the ascent prior to CI, we instead find large differences in their impact on the preconvective thermodynamic fields (Fig. 9). For example, assimilating the AERIs results in a moister cross section above 500 m AGL (+0.3 g kg^{-1}; Fig. 9a). Assimilating the composite kinematic profilers instead produces drying throughout the same layers (−0.3 g kg^{-1}; Fig. 9b). We also find that assimilating the AERIs results in weak low-level warming and midlevel cooling (Fig. 9a), whereas assimilating the composite kinematic profilers leads to slight midlevel warming throughout most of the cross section (Fig. 9b). The connection between the thermodynamic modifications and the detection of nocturnal CI is clear when comparing the assimilation impacts for convective indices (Fig. 10). The cooling and moistening in SONDE_TQPROF corresponds to increased CAPE (Fig. 10a) by ~100 J kg^{-1} for elevated parcels originating between 500 and 1000 m AGL, and slightly

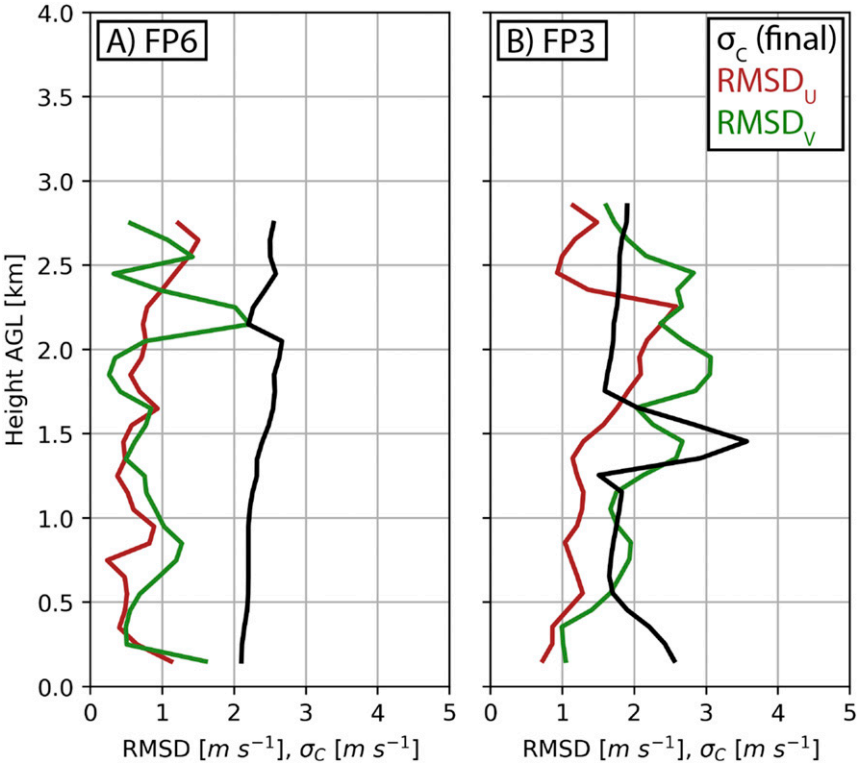

FIG. 11. Root-mean-square differences (red and green; m s^{-1}) between the composite kinematic profilers and collocated soundings launched at (a) FP6 ($n = 10$) and (b) FP3 ($n = 21$). The location for each of these sites is shown in Fig. 1a. Also overlaid is the mean, inflated observation error standard deviation (black; m s^{-1}) for the same composite kinematic observations.

reduced inhibition (Fig. 10a) by ~5 J kg^{-1} throughout the same layer. These modifications also correspond to ~150 m of less lifting required for parcels initiating between the surface and 1 km AGL to reach their level of free convection (Δz_{LFC}; Fig. 8a), though Δz_{LFC} is most strongly modified 1–3 h prior to the observed CI time. As such, the modifications made in SONDE_TQPROF result in more buoyant parcels that require less lifting to reach their LFC and are thus more likely to produce CI compared to the baseline SONDE experiment. Conversely, SONDE_UVPROF results in modifications that are largely neutral including only a small increase in CAPE (Fig. 10b), almost no decrease in CIN (Fig. 10b), and no reduction in Δz_{LFC} (Fig. 8b). These findings likely explain why assimilating the thermodynamic data results in more members being matched to the observed CI objects and overall better performance metrics, while assimilating the kinematic data likely degrades the nocturnal convective forecasts through updates to the preconvective thermodynamic state that may hinder CI.

We perform various analyses to determine why assimilating the composite kinematic profilers often results in drying and warming prior to CI, while the AERIs, which directly measure these thermodynamic variables, produce opposite effects. In Fig. 11, we compare the assigned observation error standard deviations for the kinematic profilers at FP3 and FP6 to the RMSD between the profilers and collocated rawinsondes. Because the RSMD provides a measure of the instrument error, it should always be less than the assigned error (σ_c) that includes representation factors (Janjić et al. 2018). Although three of the six kinematic profiling sites feature reasonable observation errors (FP6 shown in Fig. 11a), three other sites show an RMSD that is often greater than the assigned observation errors (FP3 shown in Fig. 11b). The underestimated observation errors at FP3 become increasingly problematic above 1.5 km AGL and could lead to erroneous observations near the top of the wind profile being weighted more heavily than they should in the DA update. As such, it is possible that these underestimated kinematic errors at some sites could contribute to updates to the thermodynamic state that oppose the collocated AERIs. However, given that the representation component of observation errors is case- and site-dependent, simply increasing the errors by a constant amount might not improve forecast results for all cases. Advanced methods are therefore needed that can diagnose flow-dependent observation errors for kinematic profilers and remote sensing instruments in general.

6. Example cases

While assimilating kinematic profilers sometimes degrades the CI forecasts, three cases also show complementary results when assimilating both the kinematic and thermodynamic

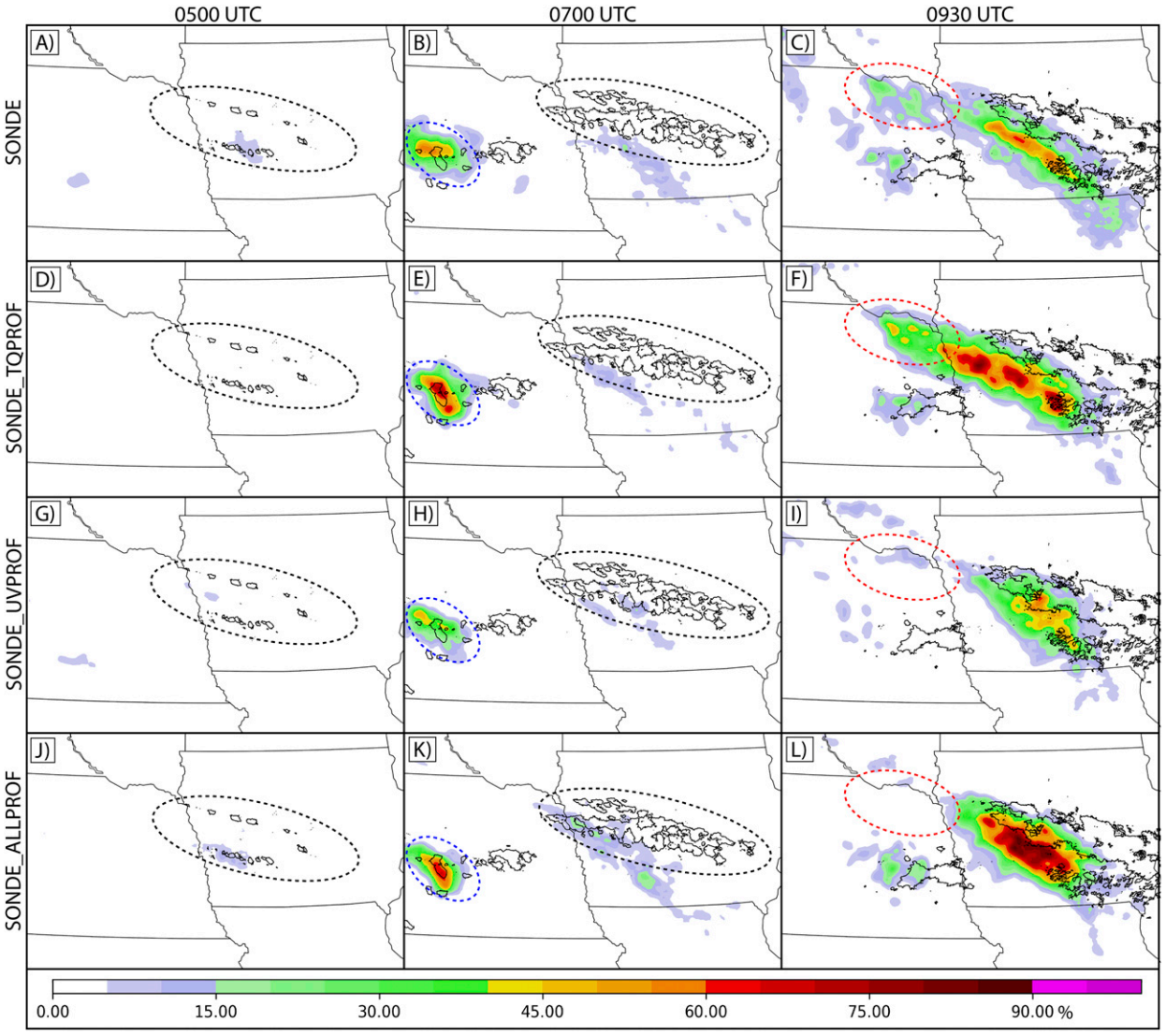

FIG. 12. Neighborhood ensemble probability of composite reflectivity exceeding 30 db*Z* for the 24 Jun frontal overrunning case valid at (a),(d),(g),(j) 0500, (b),(e),(h),(k) 0700, and (c),(f),(i),(l) 0930 UTC. Each plot is computed using an 8-km neighborhood. Also overlaid are the 30-db*Z* contours of observed composite reflectivity. See text for a description of the dashed ovals.

data together (Fig. 6). This final section explores two example cases in further detail, one that featured both datasets complementing each other such that SONDE_ALLPROF produces the best forecast of the nocturnal CI event, and one in which assimilating the composite kinematic data degrades the forecast.

a. 24 June frontal overrunning event

The 24 June event featured a large-scale CI episode that developed in central Iowa (dashed black oval in Fig. 12) near a region of isentropic ascent of the LLJ above a stationary surface boundary (Trier et al. 2020). The simulated CI was also partially generated by additional convergence both along the northern terminus of the LLJ, and along an outflow boundary generated by earlier convection in central Nebraska. Without any remote sensing data assimilated, SONDE predicts this event with low neighborhood ensemble probabilities (NEP; Schwartz and Sobash 2017) that are displaced too far south compared to the observed event at 0700 UTC (Fig. 12b). Assimilating the thermodynamic profilers increases the timing error for the initial CI event (Figs. 12a,d), but also correctly enhances the NEP values by ~20% after the simulated CI occurs (Figs. 12c,f). We note that SONDE_TQPROF also enhances the NEP values of the spurious convection in northeastern Nebraska at 0930 UTC (dashed red oval in Figs. 12c,f). Assimilating the kinematic profiles reduces the overall extent of the predicted event and suppresses much of the spurious convection produced by SONDE and SONDE_TQPROF (Fig. 12i). When both remote sensing datasets are assimilated together, SONDE_ALLPROF predicts a convective system with large NEP values (>75%) that better

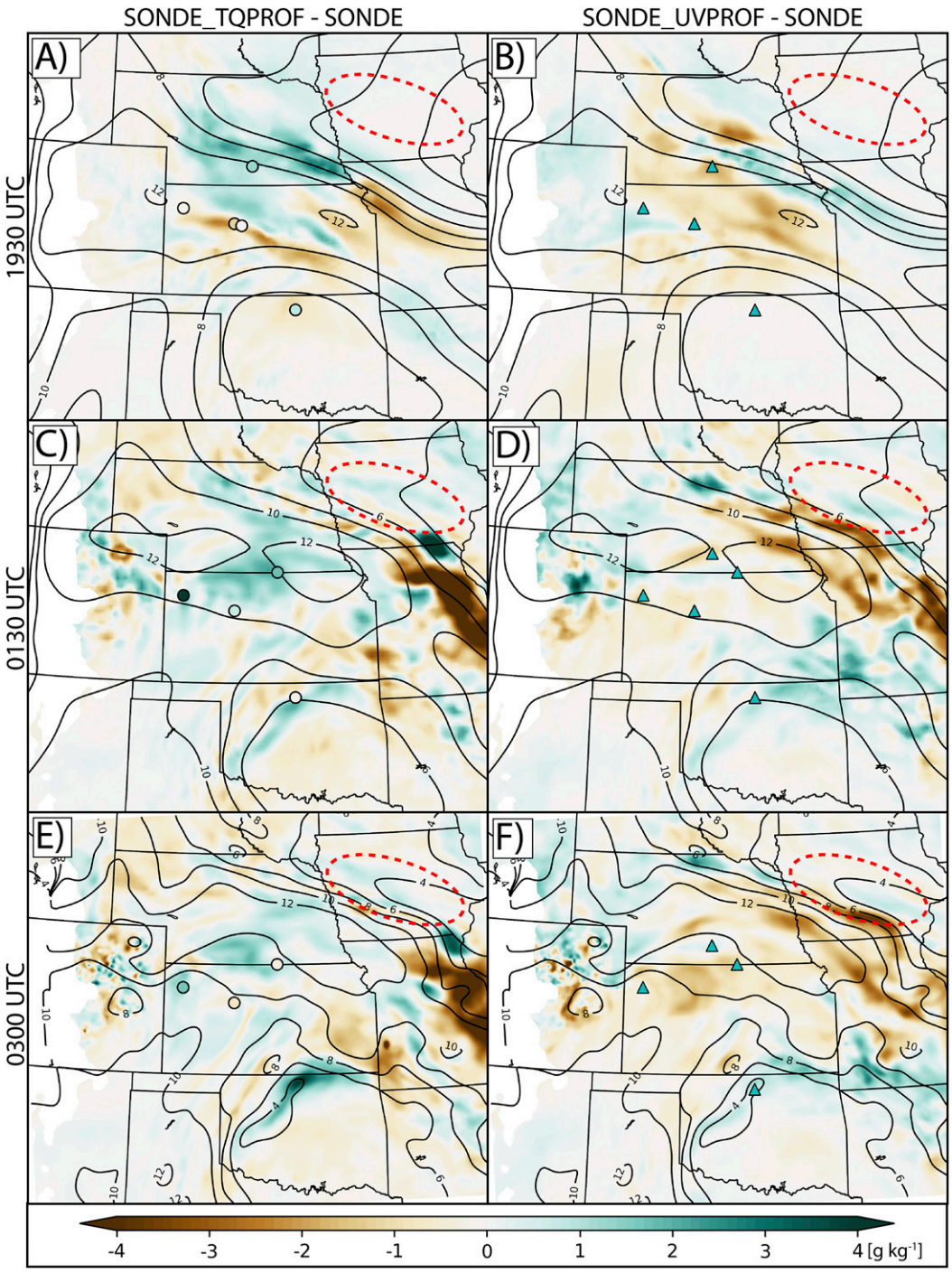

FIG. 13. Differences in 700 hPa analyzed ensemble-mean water vapor mixing ratio (g kg^{-1}) for (a),(c),(e) SONDE_TQPROF and SONDE; and (b),(d),(f) SONDE_UVPROF and SONDE. The plots are valid at (a),(b) 1930 UTC 23 Jun; (c),(d) 0130 UTC 24 Jun; and (e),(f) 0300 UTC 24 Jun. Also contoured is the ensemble-mean water vapor mixing ratio (every 2 g kg^{-1}) for SONDE. The shaded dots in (a),(c), and (e) represent innovation values (observation minus background; same color and scale as fill) for the AERI observation closest to 700 hPa and assimilated in SONDE_TQPROF. The cyan triangles in (b),(d), and (f) represent the location of composite kinematic profilers assimilated in SONDE_UVPROF. The dashed red ovals correspond to the primary location of the frontal overrunning CI event for 24 Jun.

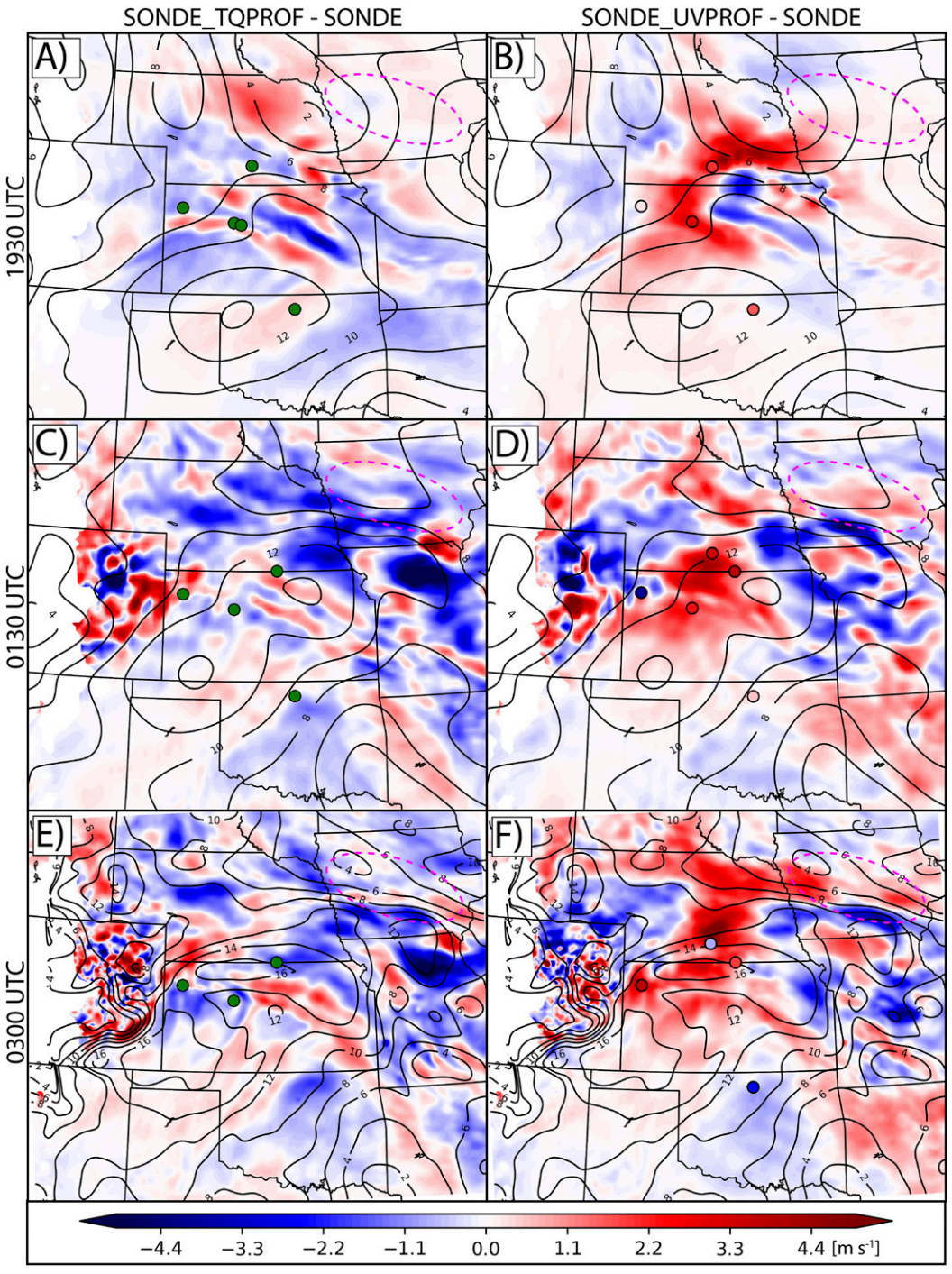

FIG. 14. As in Fig. 13, but for differences in 800-hPa analyzed wind speed (m s^{-1}). Also contoured is the ensemble-mean wind speed (every 2 m s^{-1}) for SONDE. The green dots in (a), (c), and (e) represent the location of AERI observations assimilated in SONDE_TQPROF. The shaded dots in (b), (d), and (f) represent the innovation values (observation minus background; same color and scale as fill) for the composite kinematic profiler observations closest to 800 hPa and assimilated in SONDE_UVPROF. The dashed pink ovals correspond to the primary location of the frontal overrunning CI event for 24 Jun.

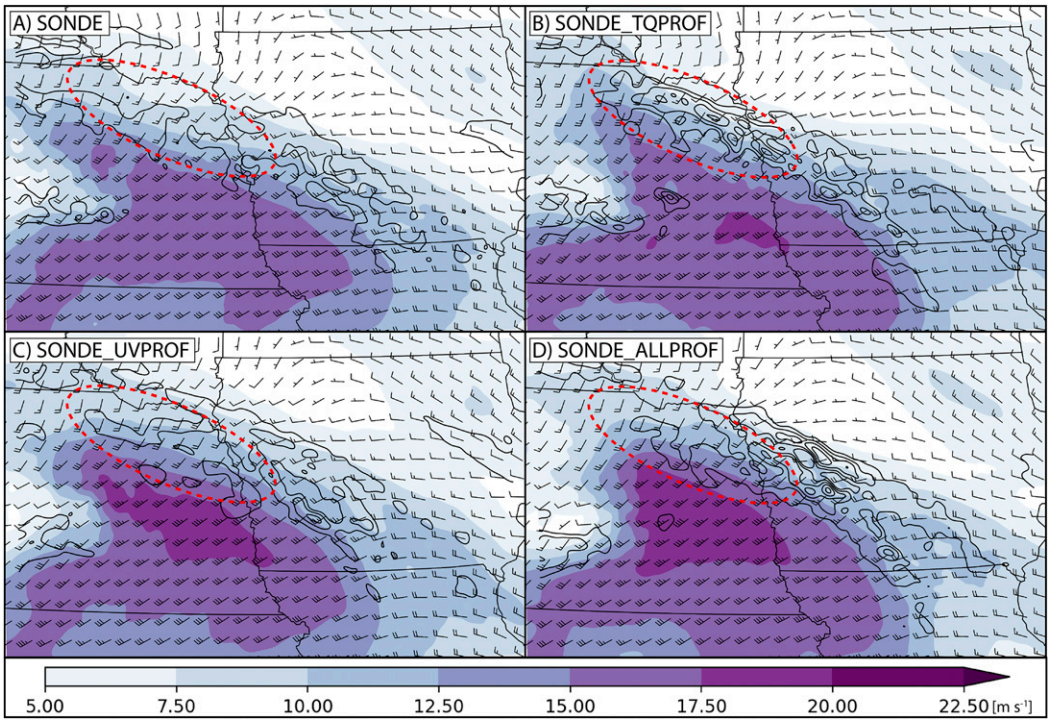

FIG. 15. Ensemble-mean forecasts of 800-hPa winds (m s^{-1}; shading and barbs) and horizontal convergence (contoured in black every $+5 \times 10^{-6}$ s^{-1}) valid at 0700 UTC 24 Jun. The half barbs represent wind speeds of 2.5 m s^{-1} and the full barbs represent wind speeds of 5 m s^{-1}. See text for a description of the dashed red ovals.

match the observed event compared to other experiments (Figs. 12c,f,i,l). We note that the 24 June case features the largest positive impact from assimilating the remote sensing data despite the observing sites being over 500 km from the CI event on average (Table 2).

We find that assimilating the thermodynamic profilers primarily enhances the convective probabilities through increased midlevel moisture near the region of CI (Fig. 13). This moisture originates from AERI observations collected between 700 and 750 hPa at FP3 and FP5. These observations show large, positive innovations and lead to differences of $\sim$+1–2 g kg^{-1} in SONDE_TQPROF during the early assimilation cycles (Fig. 13a). The southwesterly background flow then advects this additional moisture into eastern Nebraska (Figs. 13c,e) and later into the region of CI. As a result, elevated parcels in SONDE_TQPROF feature increased CAPE and reduced CIN compared to SONDE (not shown). It is also likely that this additional moisture supports the enhanced probabilities for convection in central Nebraska (dashed blue ovals in Figs. 12e,k) that later generates the strong outflow boundary responsible for spurious CI events in northeastern Nebraska (dashed oval region in Fig. 15b).

Although assimilating the kinematic profilers results in slight drying near the region of CI (Fig. 13), we instead find that these data improve the CI forecast through an enhancement of the ambient wind speed in northeastern Nebraska (Figs. 14, 15). During early DA cycles, the FP3 and MP3 wind profilers observe faster wind speeds than the ensemble backgrounds at 800 hPa (shaded dots in Figs. 14b,d). Assimilating these data causes a large increase in the wind speeds around the Kansas and Nebraska border that is then spread throughout the region of CI (Figs. 14d,f). As such, SONDE_UVPROF and SONDE_ALLPROF produce stronger wind speeds in northeastern Nebraska by $\sim$2.5 m s^{-1} during the forecast period (Figs. 15c,d). When an outflow boundary produced by earlier convection in central Nebraska passes through this region at later forecast times, the enhanced background flow weakens the speed convergence (dashed oval region in Fig. 15) and thus the extent of the spurious convection (Figs. 12c,i,l). When both remote sensing datasets are assimilated together, their impacts complement each other such that SONDE_ALLPROF features the benefits of both the enhanced moisture from assimilating the thermodynamic data and the weakened convergence that reduces the spurious convection when assimilating kinematic data (Fig. 15d). These combined effects likely explain why SONDE_ALLPROF produces the most accurate convective forecast overall (Fig. 12l).

b. 26 June frontal overrunning event

The nocturnal CI event on 26 June (detailed in section 2 of D19) featured similar ascent mechanisms to the 24 June event, including frontal overrunning by the LLJ over a stationary boundary and enhanced convergence at the terminus of the LLJ. When assimilating the thermodynamic data, we find general improvements to the CI forecast compared to SONDE, such that higher NEPs are predicted along the central portion of the

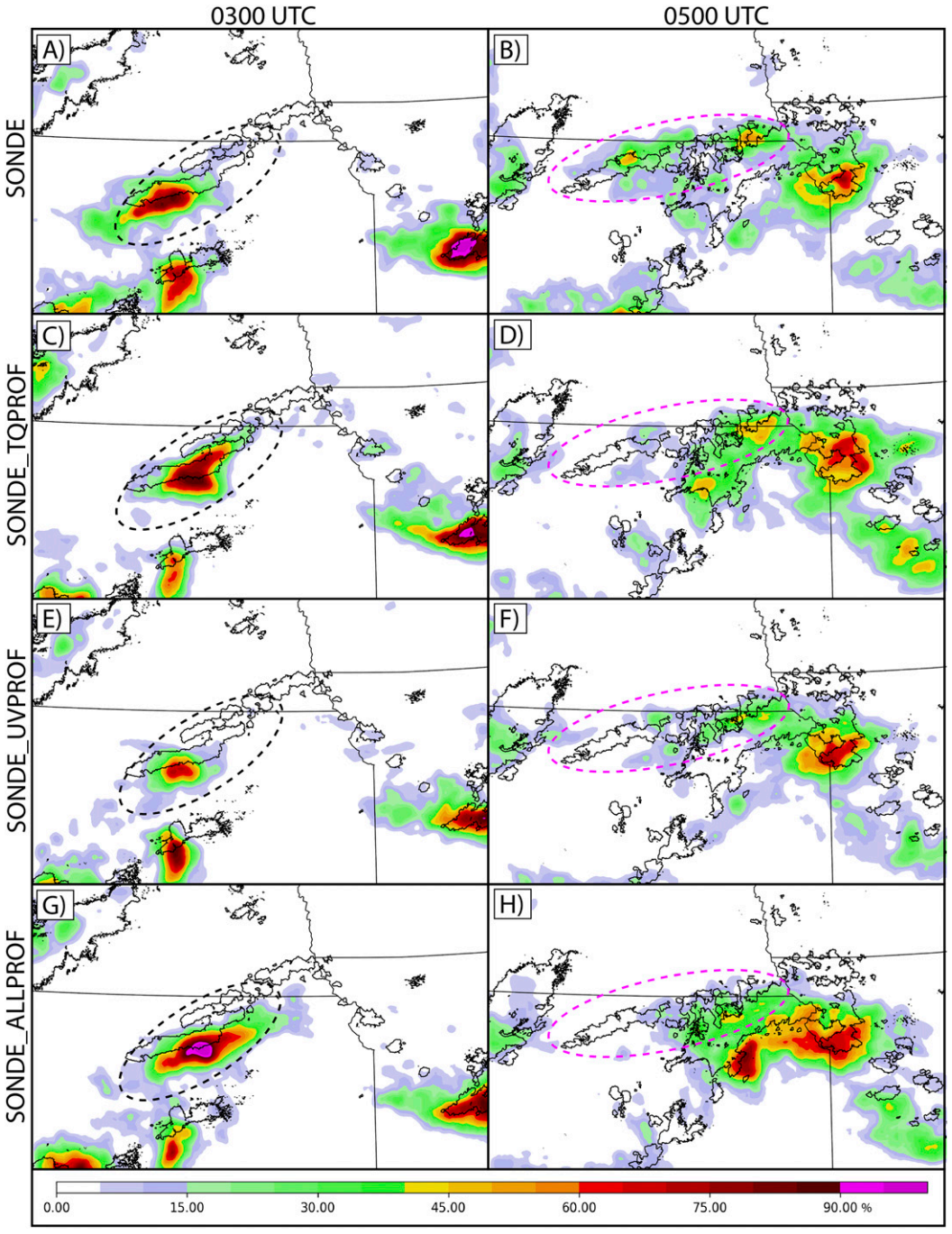

FIG. 16. As in Fig. 12, but for the 26 Jun frontal overrunning case valid at (a),(c),(e),(g) 0300 and (b),(d),(f),(h) 0500 UTC.

linear CI event and spurious convection to the southwest is suppressed (dashed black ovals in Figs. 16a,c). Conversely, SONDE_UVPROF predicts lower NEP values along most of the event (Fig. 16e). Additionally, at later forecast times when additional convection develops northwest of the main linear band, SONDE_UVPROF generates fewer convective cells and with lower probabilities compared to SONDE (dashed pink ovals in Figs. 16b,f). SONDE_ALLPROF also shows similar problems compared to SONDE_UVPROF such that the linear nocturnal CI event is predicted with a southeastern bias (Fig. 16g), and the second CI event is almost entirely missed (Fig. 16h).

As was discussed in the previous section, assimilating thermodynamic or kinematic data often has opposite effects on the preconvective moisture environment. Figure 17 demonstrates

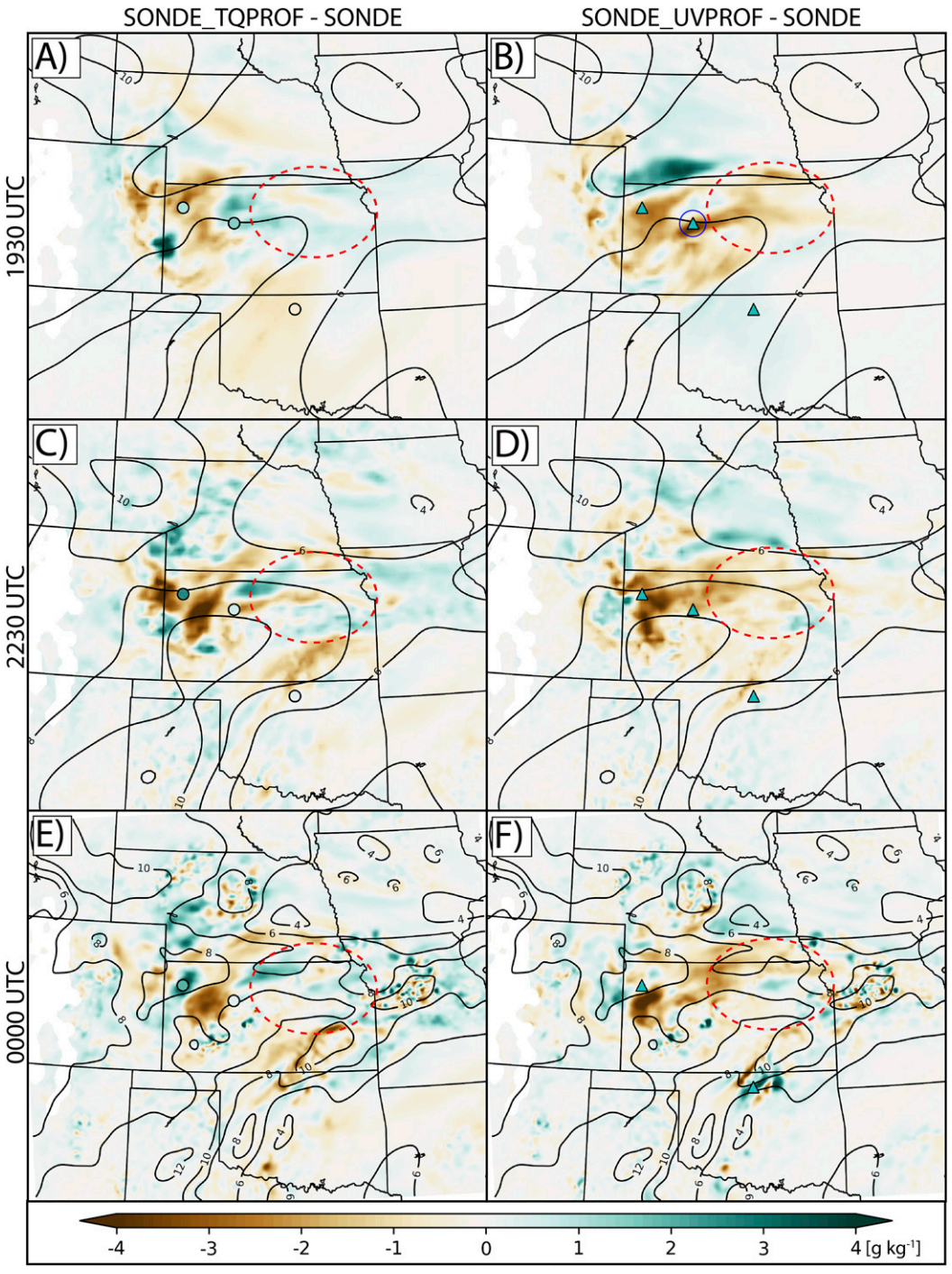

FIG. 17. As in Fig. 13 but for 750-hPa water vapor mixing ratio (g kg^{-1}) and valid at (a),(b) 1930 UTC 25 Jun; (c),(d) 2230 UTC 25 Jun; and (e),(f) 0000 UTC 26 Jun. The dashed red ovals correspond to the primary location of the frontal overrunning CI event for 26 Jun. The blue circle in (b) indicates the location of the FP3 profile shown in Fig. 18.

an example of this for the 26 June CI event. Assimilating the thermodynamic data introduces additional midlevel moisture (Fig. 17a), primarily originating from FP3, that is later advected into the region of CI and enhances the environment for new convective events (red dashed oval region in Figs. 17c,e). Conversely, assimilating the wind profiler data from the same site introduces drying that suppresses new development (Figs. 17b,d,f). We hypothesize that this drying in SONDE_UVPROF results from assimilating wind data near the top of the composite kinematic profile at FP3 (Fig. 18b). The wind observation at 1930 UTC

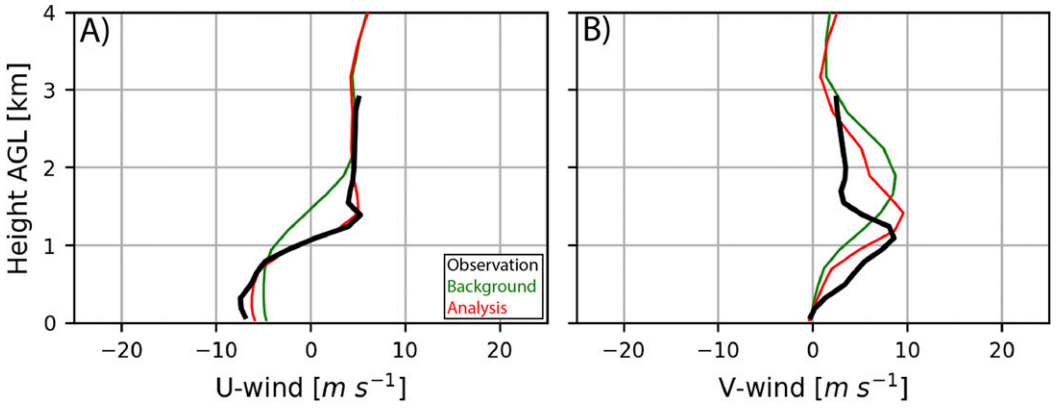

FIG. 18. Ensemble-mean background (green) and analysis (red) wind profiles for the 1930 UTC composite kinematic observation assimilated from FP3 (black; location circled in blue in Fig. 17b).

is much slower than the background wind between 700 and 800 hPa and causes a large reduction in the analyzed v wind when assimilated (Fig. 18b). Given the negative north–south moisture gradient near FP3 (Fig. 17b), assimilating this slower v wind also weakens the northward moisture advection into central Kansas. Though we have no independent observations to verify the weakened moisture advection, the convective forecast serves as an indirect verification tool. Thus, compared to the moistening and improved CI forecast that results from assimilating the thermodynamic data, we assume that the data near the top of the wind profile at FP3 are likely incorrect. Without an accurate representation of their observation errors (Fig. 11b), such data are thus likely responsible for the degraded forecast quality.

7. Summary

This study evaluates the systematic impact of assimilating a network of ground-based remote sensing instruments alongside collocated rawinsondes for 13 nocturnal CI events. The PECAN project provides a valuable dataset for determining these impacts given the diverse forcing mechanisms and environments for each case. Additionally, as most nocturnal convection is forced by mechanisms above the surface, such events serve as useful examples to understand the benefit of profiling instruments specifically. Although the limited number of nocturnal CI events sampled during PECAN prevents the estimation of statistical significance of the observation impacts, the results shown here offer valuable information compared to previous case studies that only assimilate data for one case or from a single observing site.

We find small but consistent improvements across nearly all verification metrics when assimilating thermodynamic profilers alongside collocated rawinsondes. These improvements include an increase in mean FSS in addition to improvements to standard contingency metrics such as POD, CSI, and bias. We find that assimilating the thermodynamic profiling data primarily results in midlevel cooling and moistening prior to CI, thus enhancing the likelihood of convective development and improving the detection of observed events. These results provide further evidence that a network of thermodynamic remote sensing profilers can have positive impacts on convective-scale forecasts.

Conversely, assimilating the collocated kinematic profilers often degrades the forecast performance for the detection of nocturnal CI, likely due to opposite impacts to the preconvective thermodynamic fields compared to the direct observations from the AERIs. When both datasets are assimilated together, these detriments often counteract the benefits of assimilating the thermodynamic data. However, while assimilating the kinematic data often degrades the detection of nocturnal CI, we find some forecast improvements when assimilating both datasets together. For example, the CI events that are successfully detected in SONDE_ALLPROF show lower timing, location, and orientation errors. To further improve the precise timing and location of CI, denser observing networks would likely need to be assimilated compared to the two to six sites assimilated here. Assimilating such a wider network of profilers would likely better constrain the location of convergence boundaries for which we saw little impact in this study. Finally, we also find strong variability in the impact of assimilating these datasets for different cases, likely due to the diverse mechanisms responsible for each nocturnal CI event and the number and relative location of each observing site.

We hypothesize that the forecast degradations from assimilating kinematic data are related in part to underestimated observation errors at some sites. These findings, along with the relationship between error inflation and forecast skill discussed in D19, suggest a large sensitivity between observation impacts and their assigned observation errors when assimilating high-frequency, remote sensing data. This sensitivity is likely further compounded by the large number of profilers that are assimilated at one time in this study (as many as 12 profiles from the same site during one DA cycle). As representation errors vary by environment, empirical error inflation methods such as the one applied here are likely not valid for a large set of cases. Thus, future work will examine flow-dependent methods to diagnose observation error variances for high-frequency profilers, including sampling representation errors from the background ensemble (e.g., Satterfield and Hodyss 2017), or using background and analysis-error statistics to derive optimal observation errors (e.g., Desroziers et al. 2005).

Acknowledgments. This project is primarily supported by the National Science Foundation (NSF) Award AGS-1359703 and Awards NA16OAR3420115 and NA11OAR4320072. We would also like to acknowledge the high-performance computing support from Cheyenne (doi:10.5065/D6RX99HX) provided by the Computational and Information Systems Laboratory (CISL) at the National Center for Atmospheric Research and sponsored by the NSF. We also thank Stephen Weygandt, Tammy Weckwerth, and two anonymous reviewers for providing thoughtful comments for this manuscript. Finally, the authors also wish to acknowledge the contributions from all the data providers involved in the PECAN project, as well as the members of the Multi-scale data Assimilation and Predictability Laboratory (MAP; http://weather.ou.edu/~map/index.html) at OU, especially Hristo Chipilski and Aaron Johnson, for many thoughtful discussions related to this work.

Data availability statement. The references for the remote sensing observations are given in Table 1 and the model output data for the assimilation experiments are archived locally and available upon request to the corresponding author.

REFERENCES

Adams-Selin, R., and R. S. Schumacher, 2019: Observations of low-frequency gravity waves during the PECAN field campaign. *18th Conf. on Mesoscale Processes*, Savannah, GA, Amer. Meteor. Soc., 3.5, https://ams.confex.com/ams/18MESO/meetingapp.cgi/Paper/361237.

Banta, R. M., R. K. Newsom, J. K. Lundquist, Y. L. Pichugina, R. L. Coulter, and L. Mahrt, 2002: Nocturnal low-level jet characteristics over Kansas during CASES-99. *Bound.-Layer Meteor.*, **105**, 221–252, https://doi.org/10.1023/A:1019992330866.

Benjamin, S. G., and Coauthors, 2016: A North American hourly assimilation and model forecast cycle: The Rapid Refresh. *Mon. Wea. Rev.*, **144**, 1669–1694, https://doi.org/10.1175/MWR-D-15-0242.1.

Berger, H., 2004: Satellite wind superobbing. NWPSAF-MO-VS-016, 33 pp., https://www.ssec.wisc.edu/~howardb/Papers/superob_nwpsaf_final.pdf.

Blumberg, W. G., T. J. Wagner, D. D. Turner, and J. Correia, 2017: Quantifying the accuracy and uncertainty of diurnal thermodynamic profiles and convection indices derived from the Atmospheric Emitted Radiance Interferometer. *J. Appl. Meteor. Climatol.*, **56**, 2747–2766, https://doi.org/10.1175/JAMC-D-17-0036.1.

Burghardt, B. J., C. Evans, and P. J. Roebber, 2014: Assessing the predictability of convection initiation in the high plains using an object-based approach. *Wea. Forecasting*, **29**, 403–418, https://doi.org/10.1175/WAF-D-13-00089.1.

Burlingame, B. M., C. Evans, and P. J. Roebber, 2017: The influence of PBL parameterization on the practical predictability of convection initiation during the Mesoscale Predictability Experiment (MPEX). *Wea. Forecasting*, **32**, 1161–1183, https://doi.org/10.1175/WAF-D-16-0174.1.

Calhoun, R., R. Heap, M. Princevac, R. Newsom, H. Fernando, and D. Ligon, 2006: Virtual towers using coherent Doppler lidar during the Joint Urban 2003 dispersion experiment. *J. Appl. Meteor. Climatol.*, **45**, 1116–1126, https://doi.org/10.1175/JAM2391.1.

Chipilski, H. G., X. Wang, and D. B. Parsons, 2020: Impact of assimilating PECAN profilers on the prediction of bore-driven nocturnal convection: A multiscale forecast evaluation for the 6 July 2015 case study. *Mon. Wea. Rev.*, **148**, 1147–1175, https://doi.org/10.1175/MWR-D-19-0171.1.

Clark, R., 2016: FP3 Ellis, KS radiosonde data, version 2.0. UCAR/NCAR–Earth Observing Laboratory, accessed 1 June 2019, https://doi.org/10.5065/D6GM85DZ.

Coniglio, M. C., S. F. Corfidi, and J. S. Kain, 2011: Environment and early evolution of the 8 May 2009 Derecho-producing convective system. *Mon. Wea. Rev.*, **139**, 1083–1102, https://doi.org/10.1175/2010MWR3413.1.

——, G. S. Romine, D. D. Turner, and R. D. Torn, 2019: Impacts of targeted AERI and Doppler lidar wind retrievals on short-term forecasts of the initiation and early evolution of thunderstorms. *Mon. Wea. Rev.*, **147**, 1149–1170, https://doi.org/10.1175/MWR-D-18-0351.1.

Crook, N. A., 1996: Sensitivity of moist convection forced by boundary layer processes to low-level thermodynamic fields. *Mon. Wea. Rev.*, **124**, 1767–1785, https://doi.org/10.1175/1520-0493(1996)124<1767:SOMCFB>2.0.CO;2.

Davis, C. A., B. Brown, and R. Bullock, 2006: Object-based verification of precipitation forecasts. Part II: Application to convective rain systems. *Mon. Wea. Rev.*, **134**, 1785–1795, https://doi.org/10.1175/MWR3146.1.

Degelia, S. K., X. Wang, D. J. Stensrud, and A. Johnson, 2018: Understanding the impact of radar and in situ observations on the prediction of a nocturnal convection initiation event on 25 June 2013 using an ensemble-based multiscale data assimilation system. *Mon. Wea. Rev.*, **146**, 1837–1859, https://doi.org/10.1175/MWR-D-17-0128.1.

——, ——, and ——, 2019: An evaluation of the impact of assimilating AERI retrievals, kinematic profilers, rawinsondes, and surface observations on a forecast of a nocturnal convection initiation event during the PECAN field campaign. *Mon. Wea. Rev.*, **147**, 2739–2764, https://doi.org/10.1175/MWR-D-18-0423.1.

Desroziers, G., L. Berre, B. Chapnik, and P. Poli, 2005: Diagnosis of observation, background and analysis-error statistics in observation space. *Quart. J. Roy. Meteor. Soc.*, **131**, 3385–3396, https://doi.org/10.1256/qj.05.108.

Du, J., and Coauthors, 2014: NCEP regional ensemble update: Current systems and planned storm-scale ensembles. *26th Conf. on Weather Analysis and Forecasting/22nd Conf. on Numerical Weather Prediction*, Atlanta, GA, Amer. Meteor. Soc., J1.4, https://ams.confex.com/ams/94Annual/webprogram/Paper239030.html.

Ecklund, W. L., D. A. Carter, and B. B. Balsley, 1988: A UHF wind profiler for the boundary layer: Brief description and initial results. *J. Atmos. Oceanic Technol.*, **5**, 432–441, https://doi.org/10.1175/1520-0426(1988)005<0432:AUWPFT>2.0.CO;2.

Ek, M., K. Mitchell, Y. Lin, E. Rogers, P. Grunmann, V. Koren, G. Gayno, and J. Tarpley, 2003: Implementation of Noah land surface model advances in the National Centers for Environmental Prediction operational mesoscale Eta model. *J. Geophys. Res.*, **108**, 8851, https://doi.org/10.1029/2002JD003296.

Fast, J. D., and Coauthors, 2019: Overview of the HI-SCALE field campaign: A new perspective on shallow convective clouds. *Bull. Amer. Meteor. Soc.*, **100**, 821–840, https://doi.org/10.1175/BAMS-D-18-0030.1.

Feltz, W. F., W. L. Smith, H. B. Howell, R. O. Knuteson, H. Woolf, and H. E. Revercomb, 2003: Near-continuous profiling of temperature, moisture, and atmospheric stability using the Atmospheric Emitted Radiance Interferometer (AERI). *J. Appl. Meteor.*, **42**, 584–597, https://doi.org/10.1175/1520-0450(2003)042<0584:NPOTMA>2.0.CO;2.

Geerts, B., and Coauthors, 2017: The 2015 Plains Elevated Convection At Night field project. *Bull. Amer. Meteor. Soc.*, **98**, 767–786, https://doi.org/10.1175/BAMS-D-15-00257.1.

Gero, J., H. Revercomb, D. Turner, J. Taylor, B. Ermold, K. Gaustad, R. Garcia, and D. Hackel, 2014: Atmospheric Emitted Radiance Interferometer (AERISUMMARY) from Southern Great Plains (SGP) Central Facility, Lamont, OK (C1). Atmospheric Radiation Measurement (ARM) Climate Research Facility data archive, accessed 1 June 2019, http://doi.org/10.5439/1025146.

Grell, G. A., and S. R. Freitas, 2013: A scale and aerosol aware stochastic convective parameterization for weather and air quality modeling. *Atmos. Chem. Phys.*, **13**, 23 845–23 893, https://doi.org/10.5194/acpd-13-23845-2013.

Gremillion, M. S., and R. E. Orville, 1999: Thunderstorm characteristics of cloud-to-ground lightning at the Kennedy Space Center, Florida: A study of lightning initiation signatures as indicated by the WSR-88D. *Wea. Forecasting*, **14**, 640–649, https://doi.org/10.1175/1520-0434(1999)014<0640:TCOCTG>2.0.CO;2.

Hanesiak, J., and D. Turner, 2016a: FP3 University of Manitoba Doppler lidar wind profile data, version 1.0. UCAR/NCAR–Earth Observing Laboratory, accessed 1 June 2019, https://doi.org/10.5065/D60863P5.

——, and ——, 2016b: FP6 University of Manitoba Doppler lidar VAD winds data, version 2.0. UCAR/NCAR–Earth Observing Laboratory, accessed 1 June 2019, https://doi.org/10.5065/D64F1NTN.

Hansell, R. A., and Coauthors, 2010: An assessment of the surface longwave direct radiative effect of airborne Saharan dust during the NAMMA field campaign. *J. Atmos. Sci.*, **67**, 1048–1065, https://doi.org/10.1175/2009JAS3257.1.

Holdridge, D., and D. Turner, 2015: FP6 Hesston, KS radiosonde data, version 1.0. UCAR/NCAR–Earth Observing Laboratory, accessed 1 June 2019, https://doi.org/10.5065/D6765CD0.

Hong, S., and J. J. Lim, 2006: The WRF single-moment 6-class microphysics scheme (WSM6). *J. Korean Meteor. Soc.*, **42**, 129–151.

Hu, J., N. Yussouf, D. D. Turner, T. A. Jones, and X. Wang, 2019: Impact of ground-based remote sensing boundary layer observations on short-term probabilistic forecasts of a tornadic supercell event. *Wea. Forecasting*, **34**, 1453–1476, https://doi.org/10.1175/WAF-D-18-0200.1.

Iacono, M. J., J. S. Delamere, E. J. Mlawer, M. W. Shephard, S. A. Clough, and W. D. Collins, 2008: Radiative forcing by long-lived greenhouse gases: Calculations with the AER radiative transfer models. *J. Geophys. Res.*, **113**, D13103, https://doi.org/10.1029/2008JD009944.

Janjić, T., and Coauthors, 2018: On the representation error in data assimilation. *Quart. J. Roy. Meteor. Soc.*, **144**, 1257–1278, https://doi.org/10.1002/qj.3130.

Johns, R. H., and C. A. Doswell, 1992: Severe local storms forecasting. *Wea. Forecasting*, **7**, 588–612, https://doi.org/10.1175/1520-0434(1992)007<0588:SLSF>2.0.CO;2.

Johnson, A., and X. Wang, 2017: Design and implementation of a GSI-based convection-allowing ensemble data assimilation and forecast system for the PECAN field experiment. Part I: Optimal configurations for nocturnal convection prediction using retrospective cases. *Wea. Forecasting*, **32**, 289–315, https://doi.org/10.1175/WAF-D-16-0102.1.

——, and ——, 2019: Multicase assessment of the impacts of horizontal and vertical grid spacing, and turbulence closure model, on subkilometer-scale simulations of atmospheric bores during PECAN. *Mon. Wea. Rev.*, **147**, 1533–1555, https://doi.org/10.1175/MWR-D-18-0322.1.

——, ——, J. R. Carley, L. J. Wicker, and C. Karstens, 2015: A comparison of multiscale GSI-based EnKF and 3DVar data assimilation using radar and conventional observations for midlatitude convective-scale precipitation forecasts. *Mon. Wea. Rev.*, **143**, 3087–3108, https://doi.org/10.1175/MWR-D-14-00345.1.

——, ——, and S. K. Degelia, 2017: Design and implementation of a GSI-based convection-allowing ensemble-based data assimilation and forecast system for the PECAN field experiment. Part II: Overview and evaluation of a real-time system. *Wea. Forecasting*, **32**, 1227–1251, https://doi.org/10.1175/WAF-D-16-0201.1.

——, ——, K. R. Haghi, and D. B. Parsons, 2018: Evaluation of forecasts of a convectively generated bore using an intensively observed case study from PECAN. *Mon. Wea. Rev.*, **146**, 3097–3122, https://doi.org/10.1175/MWR-D-18-0059.1.

——, ——, Y. Wang, A. Reinhart, A. J. Clark, and I. L. Jirak, 2020: Neighborhood- and object-based probabilistic verification of the OU MAP ensemble forecasts during 2017 and 2018 Hazardous Weather Testbeds. *Wea. Forecasting*, **35**, 169–191, https://doi.org/10.1175/WAF-D-19-0060.1.

Kain, J. S., and Coauthors, 2013: A feasibility study for probabilistic convection initiation forecasts based on explicit numerical guidance. *Bull. Amer. Meteor. Soc.*, **94**, 1213–1225, https://doi.org/10.1175/BAMS-D-11-00264.1.

Keclik, A. M., C. Evans, P. J. Roebber, and G. S. Romine, 2017: The influence of assimilated upstream, preconvective dropsonde observations on ensemble forecasts of convection initiation during the Mesoscale Predictability Experiment. *Mon. Wea. Rev.*, **145**, 4747–4770, https://doi.org/10.1175/MWR-D-17-0159.1.

Keene, K. M., and R. S. Schumacher, 2013: The bow and arrow mesoscale convective structure. *Mon. Wea. Rev.*, **141**, 1648–1672, https://doi.org/10.1175/MWR-D-12-00172.1.

Klein, P., D. Turner, E. Smith, and J. Gebauer, 2016: Mobile PISA 1 OU/NSSL CLAMPS radiosonde data, version 1.0. UCAR/NCAR–Earth Observing Laboratory, accessed 1 June 2019, https://doi.org/10.5065/D6416VDH.

Lakshmanan, V., T. Smith, G. Stumpf, and K. Hondl, 2007: The Warning Decision Support System–Integrated Information. *Wea. Forecasting*, **22**, 596–612, https://doi.org/10.1175/WAF1009.1.

——, K. Hondl, and R. Rabin, 2009: An efficient, general-purpose technique for identifying storm cells in geospatial images. *J. Atmos. Oceanic Technol.*, **26**, 523–537, https://doi.org/10.1175/2008JTECHA1153.1.

Lin, Y., R. D. Farley, and H. D. Orville, 1983: Bulk parameterization of the snow field in a cloud model. *J. Climate Appl. Meteor.*, **22**, 1065–1092, https://doi.org/10.1175/1520-0450(1983)022<1065:BPOTSF>2.0.CO;2.

Martin, W. J., and M. Xue, 2006: Sensitivity analysis of convection of the 24 May 2002 IHOP case using very large ensembles. *Mon. Wea. Rev.*, **134**, 192–207, https://doi.org/10.1175/MWR3061.1.

Menzies, R. T., and R. M. Hardesty, 1989: Coherent Doppler lidar for measurements of wind fields. *Proc. IEEE*, **77**, 449–462, https://doi.org/10.1109/5.24130.

Muradyan, P., 2013: Radar Wind Profiler (915RWPTEMPCON, updated hourly) from Southern Great Plains (SGP) central facility (C1), NW radar wind profiler site (I10), NE radar wind profiler site (I8). Atmospheric radiation measurement (ARM) Climate Research Facility data archive, accessed 1 June 2019, http://doi.org/10.5439/1025131.

Nakanishi, M., and H. Niino, 2006: An improved Mellor–Yamada level-3 model: Its numerical stability and application to a regional prediction of advection fog. *Bound.-Layer Meteor.*, **119**, 397–407, https://doi.org/10.1007/s10546-005-9030-8.

National Research Council, 2009: *Observing Weather and Climate from the Ground Up*. National Academies Press, 250 pp.

Newsom, R., and R. Krishnamurthy, 2014: Doppler Lidar (DLAUX) from Southern Great Plains (SGP) Central Facility, Lamont, OK (C1). Atmospheric radiation measurement (ARM) Climate Research Facility data archive, accessed 1 June 2019, http://doi.org/10.5439/1374838.

——, W. A. Brewer, J. M. Wilczak, D. E. Wolfe, S. P. Oncley, and J. K. Lundquist, 2017: Validating precision estimates in horizontal wind measurements from a Doppler lidar. *Atmos. Meas. Tech.*, **10**, 1229–1240, https://doi.org/10.5194/amt-10-1229-2017.

NOAA, 2015: Warning Decision Training Division (WDTD) virtual lab: MRMS products guide (version 10). Accessed 1 July 2020, https://vlab.ncep.noaa.gov/web/wdtd/mrms-products-guide.

O'Connor, E. J., A. J. Illingworth, I. M. Brooks, C. D. Westbrook, R. J. Hogan, F. Davies, and B. J. Brooks, 2010: A method for estimating the turbulent kinetic energy dissipation rate from a vertically pointing Doppler lidar, and independent evaluation from balloon-borne in situ measurements. *J. Atmos. Oceanic Technol.*, **27**, 1652–1664, https://doi.org/10.1175/2010JTECHA1455.1.

Orlanski, I., 1975: A rational subdivision of scales for atmospheric processes. *Bull. Amer. Meteor. Soc.*, **56**, 527–530.

Peters, J. M., E. R. Nielsen, M. D. Parker, S. M. Hitchcock, and R. S. Schumacher, 2017: The impact of low-level moisture errors on model forecasts of an MCS observed during PECAN. *Mon. Wea. Rev.*, **145**, 3599–3624, https://doi.org/10.1175/MWR-D-16-0296.1.

Reif, D. W., and H. B. Bluestein, 2017: A 20-year climatology of nocturnal convection initiation over the central and southern Great Plains during the warm season. *Mon. Wea. Rev.*, **145**, 1615–1639, https://doi.org/10.1175/MWR-D-16-0340.1.

——, and ——, 2018: Initiation mechanisms of nocturnal convection without nearby surface boundaries over the central and southern Great Plains during the warm season. *Mon. Wea. Rev.*, **146**, 3053–3078, https://doi.org/10.1175/MWR-D-18-0040.1.

Roberts, N. M., and H. W. Lean, 2008: Scale-selective verification of rainfall accumulations from high-resolution forecasts of convective events. *Mon. Wea. Rev.*, **136**, 78–97, https://doi.org/10.1175/2007MWR2123.1.

Roebber, P. J., 2009: Visualizing multiple measures of forecast quality. *Wea. Forecasting*, **24**, 601–608, https://doi.org/10.1175/2008WAF2222159.1.

Rogers, E., and Coauthors, 2009: NCEP North American mesoscale modeling system: Recent changes and future plans. *23rd Conf. on Weather Analysis and Forecasting/19th Conf. on Numerical Weather Prediction*, Omaha, NE, Amer. Meteor. Soc., 2A.4, https://ams.confex.com/ams/23WAF19NWP/techprogram/paper_154114.htm.

Romine, G. S., C. S. Schwartz, R. D. Torn, and M. L. Weisman, 2016: Impact of assimilating dropsonde observations from MPEX on ensemble forecasts of severe weather events. *Mon. Wea. Rev.*, **144**, 3799–3823, https://doi.org/10.1175/MWR-D-15-0407.1.

Satterfield, E., and D. Hodyss, 2017: Investigating the use of ensemble variance to predict observation error of representation. *Mon. Wea. Rev.*, **145**, 653–667, https://doi.org/10.1175/MWR-D-16-0299.1.

Schwartz, C. S., and R. A. Sobash, 2017: Generating probabilistic forecasts from convection-allowing ensembles using neighborhood approaches: A review and recommendations. *Mon. Wea. Rev.*, **145**, 3397–3418, https://doi.org/10.1175/MWR-D-16-0400.1.

——, G. S. Romine, K. R. Fossell, R. A. Sobash, and M. L. Weisman, 2017: Toward 1- km ensemble forecasts over large domains. *Mon. Wea. Rev.*, **145**, 2943–2969, https://doi.org/10.1175/MWR-D-16-0410.1.

Sisterson, D. L., R. A. Peppler, T. S. Cress, P. J. Lamb, and D. D. Turner, 2016: The ARM Southern Great Plains (SGP) site. *The Atmospheric Radiation Measurement (ARM) Program: The First 20 Years*, *Meteor. Monogr.*, No. 57, Amer. Meteor. Soc., https://doi.org/10.1175/AMSMONOGRAPHS-D-16-0004.1.

Skamarock, W. C., and Coauthors, 2008: A description of the Advanced Research WRF version 3. NCAR Tech. Note NCAR/TN-475+STR, 113 pp., https://doi.org/10.5065/D68S4MVH .

Skinner, P. S., L. J. Wicker, D. M. Wheatley, and K. H. Knopfmeier, 2016: Application of two spatial verification methods to ensemble forecasts of low-level rotation. *Wea. Forecasting*, **31**, 713–735, https://doi.org/10.1175/WAF-D-15-0129.1.

Smalikho, I., F. Köpp, and S. Rahm, 2005: Measurement of atmospheric turbulence by 2-μm Doppler lidar. *J. Atmos. Oceanic Technol.*, **22**, 1733–1747, https://doi.org/10.1175/JTECH1815.1.

Smith, E. N., J. G. Gebauer, P. M. Klein, E. Fedorovich, and J. A. Gibbs, 2019: The Great Plains low-level jet during PECAN: Observed and simulated characteristics. *Mon. Wea. Rev.*, **147**, 1845–1869, https://doi.org/10.1175/MWR-D-18-0293.1.

Smith, T. M., and Coauthors, 2016: Multi-Radar Multi- Sensor (MRMS) severe weather and aviation products: Initial operating capabilities. *Bull. Amer. Meteor. Soc.*, **97**, 1617–1630, https://doi.org/10.1175/BAMS-D-14-00173.1.

Smith, W. L., W. F. Feltz, R. O. Knuteson, H. E. Revercomb, H. M. Woolf, and H. B. Howell, 1999: The retrieval of planetary boundary layer structure using ground-based infrared spectral radiance measurements. *J. Atmos. Oceanic Technol.*, **16**, 323–333, https://doi.org/10.1175/1520-0426(1999)016<0323:TROPBL>2.0.CO;2.

Stalker, J., J. Lasley, G. Frederick, R. McPherson, P. Campbell, B. Philips, and B. Pasken, 2013: A nationwide network of networks. *Bull. Amer. Meteor. Soc.*, **94**, 1602–1606, https://doi.org/10.1175/1520-0477-94.10.1602.

Stelten, S., and W. A. Gallus, 2017: Pristine nocturnal convective initiation: A climatology and preliminary examination of predictability. *Wea. Forecasting*, **32**, 1613–1635, https://doi.org/10.1175/WAF-D-16-0222.1.

Tao, W.-K., and Coauthors, 2003: Microphysics, radiation and surface processes in the Goddard Cumulus Ensemble (GCE) model. *Meteor. Atmos. Phys.*, **82**, 97–137, https://doi.org/10.1007/s00703-001-0594-7.

Toms, B. A., J. M. Tomaszewski, D. D. Turner, and S. E. Koch, 2017: Analysis of a lower-tropospheric gravity wave train using direct and remote sensing measurement systems. *Mon. Wea. Rev.*, **145**, 2791–2812, https://doi.org/10.1175/MWR-D-16-0216.1.

Trier, S. B., S. D. Kehler, and J. Hanesiak, 2020: Observations and simulation of elevated nocturnal convection initiation on 24 June 2015 during PECAN. *Mon. Wea. Rev.*, **148**, 613–635, https://doi.org/10.1175/MWR-D-19-0218.1.

Turner, D., 2016a: FP3 AERIoe thermodynamic profile retrieval data, version 2.0. UCAR/NCAR–Earth Observation Laboratory, accessed 1 June 2019, https://doi.org/10.5065/D6Z31WV0.

——, 2016b: FP4 AERIoe thermodynamic profile retrieval data, version 2.0. UCAR/NCAR–Earth Observing Laboratory, accessed 1 June 2019, https://doi.org/10.5065/D6PN93T3.

——, 2016c: FP5 AERIoe thermodynamic profile retrieval data, version 2.0. UCAR/NCAR–Earth Observation Laboratory, accessed 1 June 2019, https://doi.org/10.5065/D61V5C5J.

——, 2016d: FP6 AERIoe thermodynamic profile retrieval data, version 2.0. UCAR/NCAR–Earth Observing Laboratory, accessed 1 June 2019, https://doi.org/10.5065/D6TD9VH0.

——, 2016e: MP1 OU/NSSL CLAMPS Doppler lidar VAD wind data, version 1.0. UCAR/NCAR–Earth Observing Laboratory, accessed 1 June 2019, https://doi.org/10.5065/D6BR8QJH.

——, 2018: MP1 OU/NSSL CLAMPS AERIoe thermodynamic profile retrieval data, version 1.2. UCAR/NCAR–Earth Observing Laboratory, accessed 1 June 2019, https://doi.org/10.5065/D6VQ312C.

——, and U. Löhnert, 2014: Information content and uncertainties in thermodynamic profiles and liquid cloud properties retrieved from the ground-based Atmospheric Emitted Radiance Interferometer (AERI). *J. Appl. Meteor. Climatol.*, **53**, 752–771, https://doi.org/10.1175/JAMC-D-13-0126.1.

——, and W. G. Blumberg, 2019: Improvements to the AERIoe thermodynamic profile retrieval algorithm. *IEEE Select Topics Appl. Earth Obs. Remote Sens.*, **12**, 1339–1354, https://doi.org/10.1109/JSTARS.2018.2874968.

UCAR/NCAR, 2015a: FP1 ARM central facility radiosonde data, version 1.0. UCAR/NCAR–Earth Observation Laboratory, accessed 1 June 2019, https://data.eol.ucar.edu/dataset/485.021.

——, 2015b: FP4 NCAR/EOL 915 MHz profiler NIMA consensus winds and moments, version 1.0. UCAR/NCAR–Earth Observing Laboratory, accessed 1 June 2018, https://doi.org/10.5065/D6RV0KXH.

——, 2015c: FP5 NCAR/EOL 915 MHz profiler 30 minute consensus winds and moments data, version 1.0. UCAR/NCAR–Earth Observing Laboratory, accessed 1 June 2018, https://doi.org/10.5065/D6H993DQ.

——, 2016a: FP4 NCAR/EOL QC soundings, version 2.0. UCAR/NCAR–Earth Observing Laboratory, accessed 1 June 2019, https://doi.org/10.5065/D63776XH.

——, 2016b: FP5 NCAR/EOL QC soundings, version 2.0. UCAR/NCAR–Earth Observing Laboratory, accessed 1 June 2019, https://doi.org/10.5065/D6ZG6QF7.

——, 2017: FP3 NCAR/EOL 449MHz profiler 30 minute consensus winds data, version 1.0 [PRELIMINARY]. UCAR/NCAR–Earth Observing Laboratory, accessed 1 June 2018, https://doi.org/10.5065/D66W98T7.

Wagner, T., D. Turner, and R. Newsom, 2016a: MP3 University of Wisconsin SPARC Doppler lidar VAD wind data, version 2.0. UCAR/NCAR–Earth Observing Laboratory, accessed 1 June 2019, https://doi.org/10.5065/D6V9869B.

——, E. Olson, N. Smith, and W. Feltz, 2016b: MP3 University of Wisconsin SPARC AERIoe thermodynamic profile data, version 1.0. UCAR/NCAR–Earth Observing Laboratory, accessed 1 June 2019, https://doi.org/10.5065/D60Z71HC.

——, ——, ——, and ——, 2016c: Mobile PISA 3 UW/SSEC SPARC radiosonde data, version 2.0. UCAR/NCAR–Earth Observing Laboratory, accessed 1 June 2019, https://doi.org/10.5065/D6VH5M7B.

Wang, X., D. Parrish, D. Kleist, and J. Whitaker, 2013: GSI 3DVar-based ensemble-variational hybrid data assimilation for NCEP global forecast system: Single resolution experiments. *Mon. Wea. Rev.*, **141**, 4098–4117, https://doi.org/10.1175/MWR-D-12-00141.1.

Wang, Y., and X. Wang, 2017: Direct assimilation of radar reflectivity without tangent linear and adjoint of the nonlinear observation operator in the GSI-based EnVar system: Methodology and experiment with the 8 May 2003 Oklahoma city tornadic supercell. *Mon. Wea. Rev.*, **145**, 1447–1471, https://doi.org/10.1175/MWR-D-16-0231.1.

Weckwerth, T. M., and D. B. Parsons, 2006: A review of convection initiation and motivation for IHOP_2002. *Mon. Wea. Rev.*, **134**, 5–22, https://doi.org/10.1175/MWR3067.1.

——, and U. Romatschke, 2019: Where, when, and why did it rain during PECAN? *Mon. Wea. Rev.*, **147**, 3557–3573, https://doi.org/10.1175/MWR-D-18-0458.1.

——, J. Hanesiak, J. W. Wilson, S. B. Trier, S. K. Degelia, W. A. Gallus, R. D. Roberts, and X. Wang, 2019: Nocturnal convection initiation during PECAN 2015. *Bull. Amer. Meteor. Soc.*, **100**, 2223–2239, https://doi.org/10.1175/BAMS-D-18-0299.1.

Wei, M., Z. Toth, R. Wobus, and Y. Zhu, 2008: Initial perturbations based on the Ensemble Transform (ET) technique in the NCEP global operational forecast system. *Tellus*, **60A**, 62–79, https://doi.org/10.1111/j.1600-0870.2007.00273.x.

Wilks, D. S., 2011: *Statistical Methods in the Atmospheric Sciences*. 3rd ed. International Geophysics Series, Vol. 100, Academic Press, 704 pp.

Wilson, J. W., and R. D. Roberts, 2006: Summary of convective storm initiation and evolution during IHOP: Observational and modeling perspective. *Mon. Wea. Rev.*, **134**, 23–47, https://doi.org/10.1175/MWR3069.1.